JGR Biogeosciences

RESEARCH ARTICLE
10.1029/2024JG008059

Key Points:

- In situ data and satellite remote sensing used to develop and validate a predictive model of dissolved organic carbon (DOC) concentration in tidal saltmarsh estuary
- DOC dynamics in tidal estuary were predicted accurately (within 16% of in situ DOC) from river discharge, water level, and marsh enhanced vegetation index 2
- Modeled DOC dynamics can be combined with hydrodynamic models to calculate DOC fluxes in tidal estuaries and inform carbon cycle models

Supporting Information:

Supporting Information may be found in the online version of this article.

Correspondence to:

A. Tuzcu Kokal and C. G. Fichot,
tuzcuay@itu.edu.tr;
cgfichot@bu.edu

Citation:

Tuzcu Kokal, A., Harringmeyer, J. P., Cronin-Golomb, O., Weiser, M. W., Hong, J., Ghosh, N., et al. (2024). Capturing the dynamics of dissolved organic carbon (DOC) in tidal saltmarsh estuaries using remote-sensing-informed models. *Journal of Geophysical Research: Biogeosciences*, *129*, e2024JG008059. https://doi.org/10.1029/2024JG008059

Received 2 FEB 2024
Accepted 2 SEP 2024

Author Contributions:

Conceptualization: Aylin Tuzcu Kokal, Cédric G. Fichot
Data curation: Cédric G. Fichot
Formal analysis: Aylin Tuzcu Kokal
Funding acquisition: Aylin Tuzcu Kokal, Nebiye Musaoglu, Cédric G. Fichot
Investigation: Aylin Tuzcu Kokal, Joshua P. Harringmeyer, Olivia Cronin-Golomb, Matthew W. Weiser, Jiyeong Hong, Nilotpal Ghosh, Jaydi Swanson, Xiaohui Zhu, Cédric G. Fichot
Methodology: Aylin Tuzcu Kokal, Cédric G. Fichot
Project administration: Cédric G. Fichot
Resources: Cédric G. Fichot
Supervision: Cédric G. Fichot

Capturing the Dynamics of Dissolved Organic Carbon (DOC) in Tidal Saltmarsh Estuaries Using Remote-Sensing-Informed Models

Aylin Tuzcu Kokal[1,2], Joshua P. Harringmeyer[1], Olivia Cronin-Golomb[1], Matthew W. Weiser[1], Jiyeong Hong[1], Nilotpal Ghosh[1], Jaydi Swanson[1], Xiaohui Zhu[1], Nebiye Musaoglu[2], and Cédric G. Fichot[1]

[1]Department of Earth and Environment, Boston University, Boston, MA, USA, [2]Department of Geomatics Engineering, Faculty of Civil Engineering, Istanbul Technical University, Istanbul, Türkiye

Abstract The fluxes of dissolved organic carbon (DOC) through tidal marsh-influenced estuaries remain poorly quantified and have been identified as a missing component in carbon-cycle models. The extreme variability inherent to these ecosystems of the land-ocean interface challenge our ability to capture DOC-concentration dynamics and to calculate accurate DOC fluxes. In situ discrete and continuous measurements provide high-quality estimates of DOC concentration, but these strategies are constrained spatially and temporally and can be costly to operate. Here, field measurements and high-spatial-resolution remote sensing were used to train and validate a predictive model of DOC-concentration distributions in the Plum Island Estuary (PIE), a mesotidal saltmarsh-influenced estuary in Massachusetts. A large set of field measurements collected between 2017 and 2023 was used to develop and validate an empirical algorithm to retrieve DOC concentration with a ±15% uncertainty from Sentinel-2 imagery. Implementation on 141 useable images produced a 6-year time series (2017–2023) of DOC distributions along the thalweg. Analysis of the time series helped identify river discharge, tidal water level (WL), and a marsh enhanced vegetation index 2 as predictors of DOC distribution in the estuary, and facilitated the training and validation of a simple model estimating the distribution. This simple model was able to predict DOC along the PIE thalweg within ±16% of the in situ measurements. Implementation for three years (2020–2022) illustrated how this type of remote-sensing-informed models can be coupled with the outputs hydrodynamic models to calculate DOC fluxes in tidal marsh-influenced estuaries and estimate DOC export to the coastal ocean.

Plain Language Summary The lateral transfer of DOC from tidal saltmarsh estuaries to the coastal ocean is not well represented in carbon-cycle models. These estuaries are influenced by terrestrial processes, riverine and marsh inputs, and tidal fluctuations that combine to create complex dynamics of DOC concentration and complicate the quantification of DOC fluxes used to compute carbon budgets. Here, we used a combination of field measurements and high-spatial-resolution satellite imagery to develop and test a model predicting DOC concentrations along a tidal saltmarsh estuary in Massachusetts from three environmental variables (i.e., tidal WL, river discharge, and a satellite-derived index of saltmarsh-biomass). A test using an independent data set revealed this simple model can estimate DOC concentrations within ±16% of the values measured in the laboratory. A simulation conducted for a continuous period of 3 years (15-min time step) showed that the model produced realistic DOC distributions and captured DOC dynamics adequately in the estuary. The model outputs can easily be coupled with hydrodynamic models to quantify the lateral transfer of DOC from tidal saltmarsh estuaries to the coastal ocean and inform carbon-cycle models.

1. Introduction

The lateral export of dissolved organic carbon (DOC) links watershed and saltmarsh carbon dynamics to the metabolic balance and health of the coastal ocean (Bauer et al., 2013; Najjar et al., 2018). Saltmarshes cover a significant fraction of the global land-ocean interface –including 12,775 km^2 in the USA, mostly along the Gulf and East coasts (CEC, 2016)– and efficiently sequester organic carbon belowground, accounting for an estimated 1/3 of the total ocean carbon burial (Duarte et al., 2005; McLeod et al., 2011; Nahlik & Fennessy, 2016). These saltmarshes are physically and biogeochemically connected to estuaries and to the continental shelf through material exchange driven by tides, storms, and other estuarine processes (Chalmers et al., 1985; Macreadie et al., 2013). Importantly, estuarine dynamics drive the lateral export of DOC from the watershed and marsh to the

Validation: Aylin Tuzcu Kokal
Visualization: Aylin Tuzcu Kokal, Cédric G. Fichot
Writing – original draft: Aylin Tuzcu Kokal, Cédric G. Fichot
Writing – review & editing: Aylin Tuzcu Kokal, Joshua P. Harringmeyer, Olivia Cronin-Golomb, Matthew W. Weiser, Jiyeong Hong, Nilotpal Ghosh, Jaydi Swanson, Xiaohui Zhu, Nebiye Musaoglu, Cédric G. Fichot

continental shelf, where it can fuel heterotrophy, provide secondary nutrients for primary production, affect the light field, act as a vector of contaminants, and influence the metabolic balance of the coastal ecosystem (Bianchi, 2011; Gattuso et al., 1998; Smith & Hollibaugh, 1993). This lateral export also has the net effect of decreasing carbon burial rates in saltmarshes, as most of the DOC exported to the coastal ocean is eventually mineralized (Fichot & Benner, 2014; Hedges et al., 1997). Globally, estuaries and saltmarshes play a disproportionately large role exchanging carbon with the coastal ocean (Herrmann et al., 2015; Najjar et al., 2018).

Despite their documented significance, fluxes of DOC through tidal marsh-influenced estuaries remain poorly quantified, leaving a critical gap in our understanding of regional and global carbon models (Benway et al., 2016; Najjar et al., 2018). The highly dynamic and heterogenous nature of these nearshore systems and the occurrence of multiple organic-carbon sources complicate quantitative assessments (Najjar et al., 2018). Estuaries also mineralize or flocculate variable fractions of DOC before export to the continental shelf, adding further complexity (Bianchi et al., 2004; Moran et al., 1999; Najjar et al., 2018; Yan et al., 2020). Differences in the geography and hydrology of estuaries and saltmarshes also make it challenging to generalize results across systems. Furthermore, this lateral conduit of DOC can be subject to long-term change as climate perturbations and human activities impact saltmarshes (Macreadie et al., 2013; Morris et al., 2013). Quantifying the lateral export of DOC and assessing its sensitivity to environmental change requires strategies that can adequately capture the hydrodynamic complexity and extreme DOC variability inherent to these systems. High-quality field observations of DOC concentration are labor-intensive and are generally too constrained in space and time to facilitate realistic DOC flux assessments. In situ fluorescence sensors can provide DOC estimates at suitable temporal resolutions (e.g., minutes to hours) but these remain spatially constrained (Menendez et al., 2022).

High-spatial-resolution remote sensing (HSRRS) offers new opportunities to complement these strategies by providing spatially explicit retrievals of DOC concentration over multiple years, although challenges remain (Fichot et al., 2023). Medium-resolution ocean-color remote sensing (e.g., MODIS, MERIS, VIIRS) with quasi-daily coverage have been used to study DOC dynamics on the nearshore continental shelf and in very large estuaries (Cao et al., 2018; Fichot et al., 2014; Mannino et al., 2008; Matsuoka et al., 2017). In a few cases, DOC retrievals have been coupled with physical models to calculate cross-shelf DOC fluxes (Joshi et al., 2017; Mannino et al., 2016; Signorini et al., 2019). However, the spatial sampling of medium-resolution sensors (250–1,000 m) is generally too coarse for application in most marsh-influenced estuaries. Over the past decade, HSRRS has become increasingly popular for studying nearshore and inland water quality (Brewin et al., 2023) and has recently been used to assess the drivers of DOC dynamics and other water constituents (e.g., total suspended solids (TSS)) in tidal marsh-influenced estuaries (Cao & Tzortziou, 2021; Zhang et al., 2020). However, the sporadic temporal coverage of these sensors (5 days at best) continues to limit the applicability of HSRRS imagery for calculating accurate DOC fluxes in these systems (Fichot et al., 2023).

Here, we leveraged >5 years (2017–2023) of HSRRS data from the Sentinel-2A/B Multispectral Instrument (MSI) tandem to elucidate the drivers of DOC dynamics in the Plum Island Estuary—a mesotidal marsh-influenced estuary in Massachusetts—and to develop a simple but reliable predictive model of DOC concentration along the estuary thalweg. A large data set of in situ measurements of DOC concentration, CDOM absorption coefficient, and remote-sensing reflectance collected from 2017 to 2023 was used to develop and validate a local DOC algorithm applicable to the Sentinel-2A/B MSI sensors. The uncertainty of DOC concentration retrieved from Sentinel-2 MSI was determined using simultaneous in situ match-up measurements, and the algorithm was implemented on all clear-sky Sentinel-2A/B scenes collected between January 2017 and July 2023. The DOC concentrations remotely sensed along the estuary thalweg were used to develop and validate the predictive *thalweg-DOC model* using river discharge, water level, and a saltmarsh biomass index as predictors, and the model was validated using in situ DOC measurements. This *thalweg-DOC model* can be implemented and coupled with the outputs of hydrodynamic models to calculate DOC fluxes within and out of tidal saltmarsh estuaries (Fagherazzi et al., 2014; Zhang et al., 2019). This study demonstrates the potential of HSRRS data to augment existing strategies and facilitate the calculation of DOC fluxes in tidal saltmarsh estuaries.

2. Study Site

The temperate PIE in Massachusetts was the site selected for this study (Figure 1). The PIE is a bar-built, mesotidal estuary that extends over about 40 km^2 and harbors the largest intertidal marsh in the northeastern USA. Two-third of the PIE area is occupied by an intertidal saltmarsh dominated by high marsh vegetated with *Spartina*

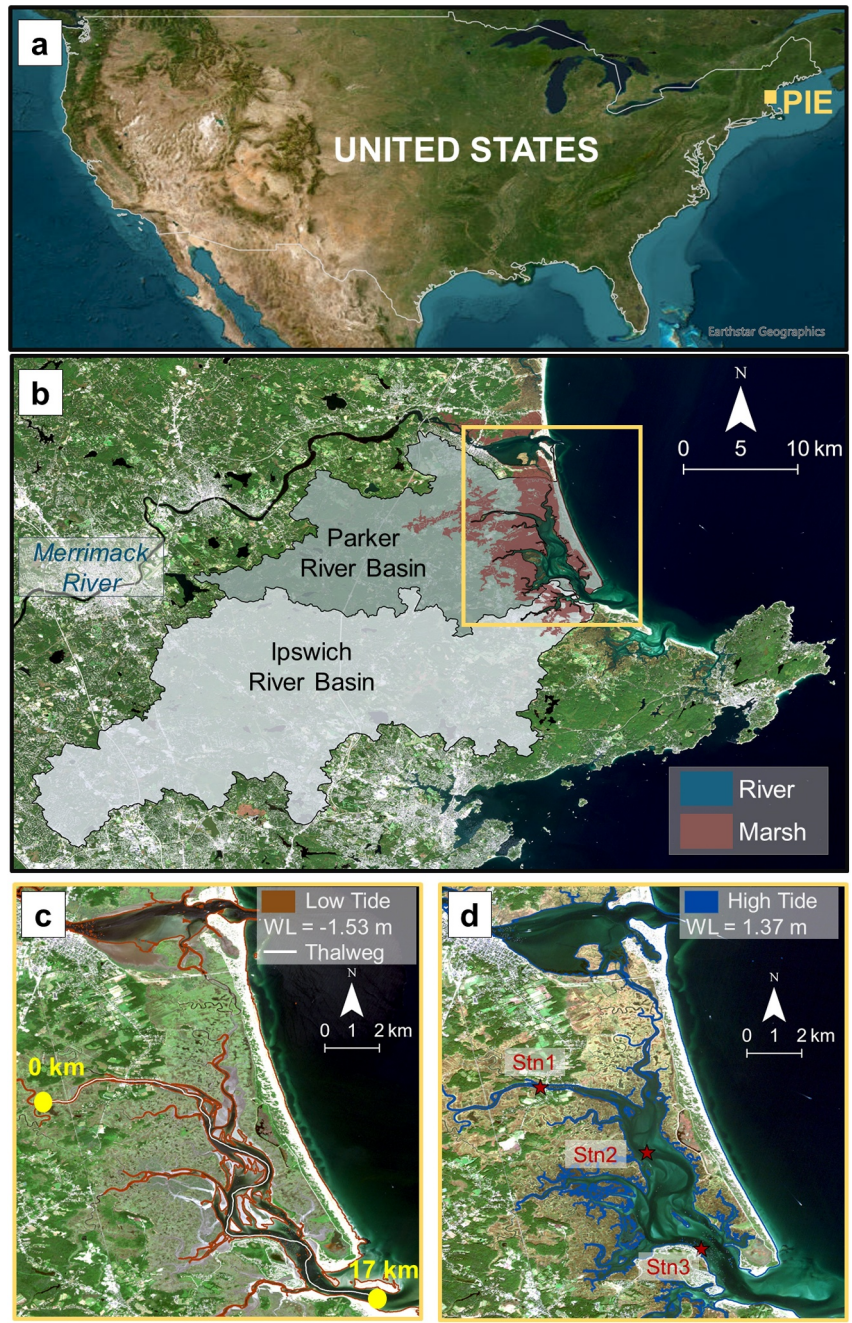

Figure 1. Study area. (a) Location of the Plum Island Estuary (PIE) in the Northeastern United States of America. (b) The PIE and surrounding areas showing the extent of the marsh and the drainage basins of the Parker and Ipswich rivers. The Merrimack River flows north of the estuary and has limited interaction with PIE through Plumbush Creek. (c) Close-up view of the PIE at low tide when the water level (WL) was 1.53 m below mean sea level (Sentinel-2 image from 19th July 2018). The red outline shows the water extent at low tide and highlights the intertidal flats. The white line shows the downstream-running estuary thalweg, over which remotely sensed dissolved organic carbon (DOC) were retrieved and analyzed, along with the corresponding initial and final distances (see Figure 13). (d) Close-up view of the PIE at high tide, when the WL was 1.37 m above mean sea level (Sentinel-2 image from 27th September 2019). The blue outline shows the water extent at high tide. The red stars show the stations used in the analysis of the modeled DOC (see Figure 16). The maps were generated using the ArcGIS Pro® software (Esri, n.d.).

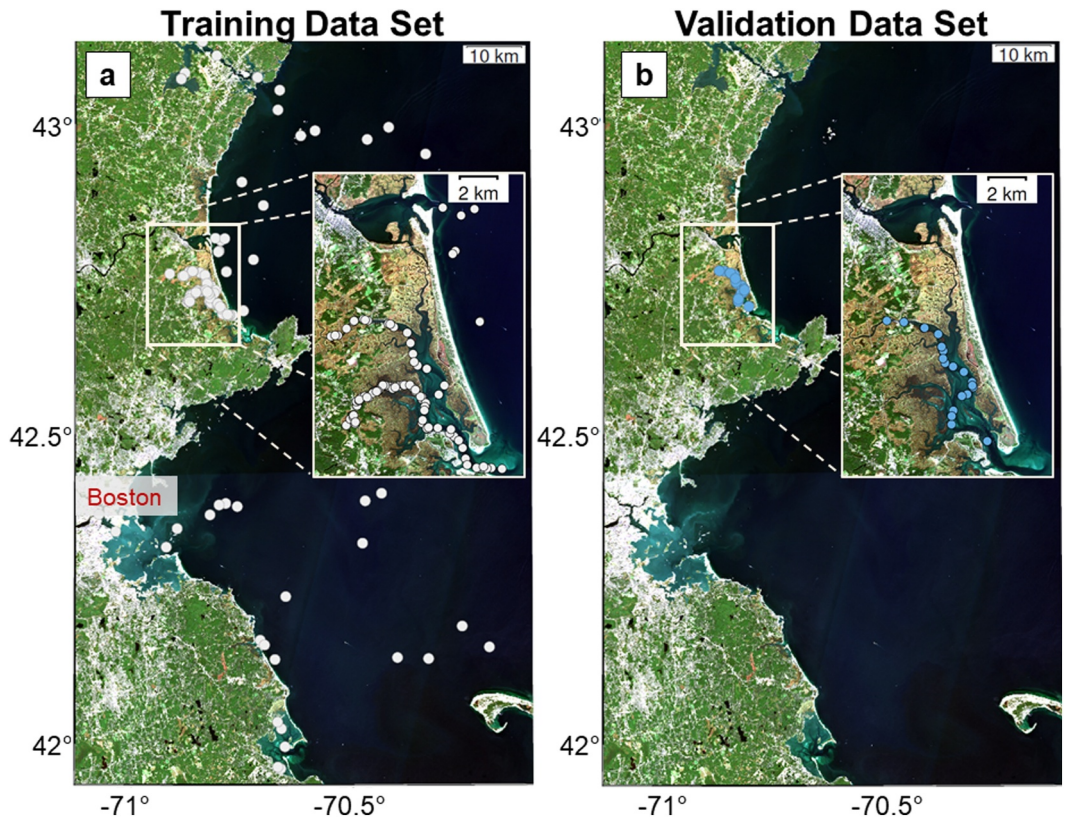

Figure 2. Location where field measurements and samples were collected between 2017 and 2023 and used for analyses, the training and validation of the algorithms, and the validation of the *thalweg-DOC model*. (a) Locations associated with the training data set collected mostly at the Plum Island Estuary (PIE), but also in Great Bay, Boston Harbor, Massachusetts Bay, and the Gulf of Maine between 2017 and 2023. (b) Locations associated with the validation data set collected strictly near the thalweg of the PIE between 2020 and 2023 coincidently to different Sentinel-2 overpasses. The maps shown here were generated using the ArcGIS Pro® software.

patens and *Distichilis spicata* (Forbrich et al., 2018). The PIE drains into the Gulf of Maine and is fed by two main rivers (Parker River and Ipswich River) and includes multiple tidal creeks (e.g., Rowley River). Limited water exchange with the Merrimack River occurs to the north of the estuary via the Plumbush creek (Zhao et al., 2010). The 609-km^2 PIE watershed includes forests, agricultural lands, swamps, and built-up areas. With a mean semi-diurnal tidal range of 3 m (Fagherazzi et al., 2014), the PIE is a well-mixed, and optically and hydrodynamically complex estuary with strong variability in salinity associated with seasons and tidal cycles (Vallino & Hopkinson, 1998; Zhao et al., 2010). The PIE region is part of the Boston Metropolitan Statistical area and hosts the Plum Island Ecosystems Long Term Ecological Research (PIE-LTER) site (https://pie-lter.ecosystems.mbl.edu/welcome-plum-island-ecosystems-lter).

3. Materials and Methods

3.1. Sampling Overview

Field samples were collected between 2017 and 2023—primarily in the spring, summer, and fall—in the PIE and in other locations in the Massachusetts Bay region of the Gulf of Maine (Figure 2). Field measurements were collected in diverse environments from narrow river channels and saltmarsh creeks to semi-enclosed bays and the continental shelf. Samples covered a wide range of estuarine and coastal conditions (Salinity 0.15–32.39) from low-turbidity and moderate-DOC shelf waters to high-turbidity and high-DOC brackish and fresh waters located nearshore and inland (Table 1). Although they were all collected near the surface (~0.5 m), the samples are expected to be representative of the water column (for DOM at least) because the PIE is characterized by a well-mixed circulation resulting from a combination of relatively large tides, shallow depth and moderate riverine

Table 1
Range, Mean, and Median Values of All In Situ and Laboratory Measurements Used in the Dissolved Organic Carbon Algorithm Development and Validation, and in the Thalweg-DOC Model Development and Cross-Validation

	Salinity	Temperature [°C]	DOC [μmol L^{-1}]	Turbidity [FNU]	*fChl-a* [RFU]	$a_g(250)$ [m^{-1}]	$a_g(340)$ [m^{-1}]	$a_g(412)$ [m^{-1}]	$a_g(490)$ [m^{-1}]	$K_d(340)$ [m^{-1}]	$K_d(412)$ [m^{-1}]	$K_d(490)$ [m^{-1}]
n	167	168	175	140	40	175	175	175	175	164	164	164
Range	0.15–32.39	5.91–26.55	79.7–888.3	0.10–9.61	0.25–2.12	3.79–99.50	0.62–32.52	0.18–10.46	0.04–3.53	0.80–41.37	0.32–14.83	0.16–5.83
Mean	27.96	15.99	233.8	2.13	1.01	19.27	5.33	1.67	0.53	6.78	2.57	1.09
Median	30.15	15.18	173.3	1.71	0.98	11.67	2.96	0.93	0.29	4.27	1.77	0.77

inputs (Vallino & Hopkinson, 1998; Zhao et al., 2010). Turbidity and chlorophyll-a concentration also varied substantially in the data set, driven by different particle sourcing in these complex estuarine and coastal environments.

3.2. In Situ Measurements and Laboratory Analyses

3.2.1. Indicators From Water-Quality Sonde

Site coordinates and in situ water quality indicators were collected at the surface (~0.5 m deep) using either a Yellow Springs Instruments (YSI) ProDSS for samples from 2017 through 2021, an EXO3 sonde for samples collected in 2022, and an EXO2 for samples collected in 2023. Each sonde was outfitted with a handheld device, an onboard GPS, a depth sensor, and sensors measuring: (a) salinity and temperature [°C], (b) turbidity [FNU], and (c) chlorophyll-a fluorescence (*fChl-a*) [RFU]. At the beginning of each field day, the depth sensor was calibrated to account for daily differences in barometric pressure, humidity, and temperature. All other sensors were calibrated in the laboratory approximately every 3 months according to manufacturer's recommendations. At each location, data was collected at a rate of 1 Hz for 60–90 s. Measurement data from all stations were manually inspected and processed using a MATLAB® (MathWorks, 2021) script to remove outliers and produce average values for each parameter at each station (Fichot et al., 2022; Harringmeyer et al., 2024).

3.2.2. Above-Water Remote-Sensing Reflectance (PSR-1100f Hyperspectral $R_{rs}(\lambda)$)

Remote sensing reflectance (R_{rs}) was measured at field stations using a Spectral Evolution Portable Spectral Radiometer (PSR-1100f) and following the above-water approach described in Harringmeyer et al. (2024). Briefly, calibrated radiance was measured from three targets: (a) A highly reflective Spectralon® Lambertian panel (L_{panel}), (b) the sky at 135° from the solar principal plane 40° from zenith (L_{sky}), and (c) the water 135° from the solar principal plane 40° from nadir ($L_{\text{water+sky}}$). Radiance was measured with 3-nm spectral sampling and interpolated to 1-nm intervals from 395 to 710 nm. Remote sensing reflectance was then calculated as in Equation 1:

$$R_{rs}(\lambda) = \frac{L_{\text{water+sky}(\lambda)} - \rho * L_{\text{sky}}(\lambda)}{\pi * L_{\text{panel}}(\lambda)/R_{\text{panel}}(\lambda)} \quad (1)$$

where R_{panel} was the manufacturer-provided reflectivity of the reference panel (>99%), λ was the measurement wavelength, and ρ was the fraction of skylight reflected at the air-water interface. The reflected fraction of incident skylight was estimated using lookup tables created by Zhang et al. (2017) based on the viewing geometry, solar zenith angle, and field-measured wind speed and assuming no cloud cover and an aerosol optical thickness of 0.06 at 550 nm, a reasonable average value for this area (Cronin-Golomb et al., 2022).

Each target radiance spectrum was measured multiple times (4–6 times), outliers were removed, and the median spectrum from each target was used to calculate $R_{rs}(\lambda)$ as in Harringmeyer et al. (2024). Care was taken during measurement to avoid reflection or shading from the boat, and measurements were collected over as short a duration as possible to minimize the influence of changing sky and wind conditions. A Savitzky-Golay filter (frame size 13, polynomial order 4) was applied to smooth the R_{rs} spectra (Vandermeulen et al., 2017).

3.2.3. In-Water Remote-Sensing Reflectance (C-OPS Multispectral Rrs(λ))

R_{rs} was also measured following an in-water approach using a Biospherical® Compact Optical Profiler System (C-OPS). The C-OPS profiler measured downwelling plane irradiance, $E_d(z)$, and upwelling radiance, $L_u(z)$, at a given depth z, simultaneously with downwelling above-water radiance measured by the surface reference sensor. Each C-OPS sensor measured radiance or irradiance at a rate of 15 Hz at 18 wavelengths between 305 nm (ultraviolet-B) and 710 nm (near-infrared). At each station, the C-OPS profiler was brought to the surface at least 5 m away on the sunward side of the boat, and the in-water radiometry was collected during freefall over several casts. Profiles of $E_d(z)$ and $L_u(z)$ were created at each station by combining at least three casts and filtering for outliers, measurements impacted by bottom reflectance, and measurements where profiler tilt was >5°. A self-shading correction (Gordon & Ding, 1992; Zibordi et al., 2015) was applied to $L_u(z)$ using total absorption coefficient spectra estimated from the diffuse attenuation coefficient spectra measured with the C-OPS at the corresponding wavelength and stations (see Section 3.2.5 below). The $L_u(z)$ and $E_d(z)$ at 13 narrow bands from 412 to 710 nm were extrapolated to the water-air interface using a quadratic fit, and an empirical relationship was applied to correct for reflection across the water air interface to calculate R_{rs} (Antoine et al., 2013; Hooker et al., 2013) as in Equation 2:

$$R_{rs}(\lambda) = \frac{L_u^{0+}(\lambda)}{E_d^{0+}(\lambda)} \tag{2}$$

Downwelling irradiance from the above-water reference sensor was used to correct for changes in illumination conditions during profile collection, as recommended in Zibordi et al. (2012).

3.2.4. Calculation of Sentinel-2-Equivalent Remote-Sensing Reflectances

In situ $R_{rs}(\lambda)$ measured using the above-water (PSR-1100f) and in-water (C-OPS) approaches described above were used to calculate $R_{rs}(\lambda)$ matching the Sentinel-2 MSI bands for algorithm development and validation. Briefly, the Sentinel-2 equivalent $R_{rs}(\lambda)$ were then calculated from the in situ $R_{rs}(\lambda)$ spectra using Equation 3:

$$\overline{R_{rs}}(\lambda_C) = \frac{\sum_{\lambda_1}^{\lambda_2} R_{rs}(\lambda_i)\,\mathrm{RSR\_C}(\lambda_i)}{\sum_{\lambda_1}^{\lambda_2} \mathrm{RSR\_C}(\lambda_i)} \tag{3}$$

where $\overline{R_{rs}}(\lambda_C)$ was the Sentinel-2 MSI-equivalent $R_{rs}(\lambda)$ for any Sentinel-2 band C (ranging from λ_1 to λ_2), $R_{rs}(\lambda_i)$ is the hyperspectral (1-nm resolution) in situ remote-sensing reflectance spectrum, and RSR_C(λ_i) is the relative spectral response of the Sentinel-2 band C obtained from the Copernicus website (ESA, 2023). The in situ $R_{rs}(\lambda)$ spectra measured using the above-water approach (PSR-1100f, 1-nm spectral resolution) were suitable for calculating broadband Sentinel-2-equivalent $\overline{R_{rs}}(\lambda_C)$. However, the majority of in situ $R_{rs}(\lambda)$ measurements were collected using the multispectral in-water approach (C-OPS), which has different and narrower bands than the Sentinel-2 MSI. The multispectral C-OPS $R_{rs}(\lambda)$ spectra were therefore interpolated to a 1-nm resolution between 395 and 800 nm. This spectral interpolation was informed by a comparative analysis of the in-water and above-water $R_{rs}(\lambda)$ at stations where both measurements were available ($n = 57$). This comparative analysis helped develop a spline interpolation that reproduced hyperspectral $R_{rs}(\lambda)$ measurements between C-OPS bands better than a linear interpolation. This interpolation of the C-OPS $R_{rs}(\lambda)$ is described in more detail in the Supporting Information (Figures S1–S2 in Supporting Information S3, and Text S1 in Supporting Information S1).

3.2.5. Diffuse Attenuation Coefficient Spectra

The C-OPS in-water $E_d(z)$ profiles were also used to calculate the diffuse attenuation of downwelling plane irradiance (K_d) at 18 wavelengths from 305 to 710 nm as described in Cronin-Golomb et al. (2022). For each profile, the slope of a linear fit between $ln(E_d(z))$ and depth was used to calculate K_d at each wavelength. Measurements outside of a manually selected depth range were filtered out to minimize the influence of noise near the surface or bottom.

3.2.6. CDOM Absorption Coefficient Spectra

Filtered (glass-fiber filters (GFF), nominal pore size 0.7 μm) water samples were equilibrated to room temperature and analyzed for CDOM absorbance on a Perkin-Elmer Lambda 650 UV/Visible dual-beam spectrophotometer. Spectra were measured at 1-nm intervals from 250 to 800 nm against a reference blank of Milli-Q water (Millipore Milli-Q Direct 16) and using acid-washed and dried 10-cm pathlength cylindrical quartz cells. Spectra were then fit using an exponential curve over the 500–700 nm range. The intercept term was used to determine a scalar offset that was subtracted from the entire spectrum, and offset-corrected absorbances were the converted to Napierian CDOM absorption coefficients, $a_g(\lambda)$, reported in [m^{-1}] (Fichot & Benner, 2011; Zhu et al., 2020).

3.2.7. DOC Concentration

Samples were analyzed for DOC concentration using high-temperature combustion with a Shimadzu TOC-L Total Organic Carbon analyzer following established methods (Fichot & Benner, 2011). Briefly, for each sample, 12–16 mL of filtered water was aliquoted into 24 mL pre-combusted (450°C for 6 hr) vials, acidified to pH ≈ 2.5 and kept in the dark until analysis, generally within a couple of weeks from collection. Duplicates of each sample were run against a pre-measured standard sample to assess instrument drift and calibrated against a glucosamine hydrochloride (Alfa Aesar) standard curve and measured in non-purgeable organic carbon (NPOC) units before being converted to μmol L^{-1} measurements using a MATLAB script. Duplicates measurements were averaged for final DOC concentrations.

3.2.8. Algal and Non-Algal Particle Absorption Coefficient Spectra

Water samples for measuring algal and non-algal absorption coefficient were collected using a 4-L Van Dorn sampler, and the entire sample was immediately transferred to a 4-L amber polyethylene bottle and stored at 4°C until filtration. Samples were gently inverted to resuspend particles, and filtered through a 25-mm diameter GFF (nominal pore size 0.7 μm). Filters and particles were flash-frozen in liquid nitrogen, and stored immediately at −80°C until laboratory analysis. Protocols for measuring algal and non-algal particle absorption coefficient spectra were adapted from standard methodologies (Neeley & Mannino, 2018; Stramski et al., 2015) and are described in detail in Harringmeyer et al. (2024). Briefly, particle absorption coefficient (a_p) was measured at 1-nm intervals from 250 to 800 nm with a Perkin-Elmer Lambda 650 UV/Visible dual-beam spectrophotometer using the inside-sphere method (Stramski et al., 2015) and a 15-cm diameter integrating sphere (Stramski et al., 2015). Filters were then soaked in methanol for 15 min to remove algal pigments, rinsed with Milli-Q water, and remeasured to determine the non-algal particle absorption coefficient (a_d). The absorption coefficient of algal particles (phytoplankton) was calculated by difference: $a_{ph} = a_p – a_d$.

3.3. Thalweg-DOC Model

3.3.1. Approach Overview

The *thalweg-DOC model* development integrated in situ measurements, HSRRS data, and environmental monitoring data (Figure 3). First, the in situ $R_{rs}(\lambda)$, CDOM absorption coefficient, and DOC concentration measured between 2017 and 2023 were divided into training and validation subsets and used to develop and validate a local remote-sensing DOC-algorithm. The validated DOC-algorithm was then implemented on 6 different clear-sky and atmospherically corrected Sentinel-2 images for which coincident (±1.5 hr), collocated in situ measurements of $R_{rs}(\lambda)$, CDOM, and DOC were available. This match-up analysis facilitated validation of the Sentinel-2 DOC retrievals. Second, the DOC-algorithm was applied to a library of 141 clear-sky and atmospherically corrected Sentinel-2 images collected during various conditions. The remotely sensed DOC concentrations were extracted along the estuary thalweg for each Sentinel-2 image to create 141 representative transects of DOC concentration. Here, data were only extracted along the thalweg because it is the deepest part of the estuary and the least likely to be influenced by bottom reflectance at low tide, and because the PIE is a well-mixed mesotidal estuary (Hopkinson et al., 2018), leading to low heterogeneity across the deeper part of the channel. Third, the remotely sensed DOC transects were used to develop and validate the *thalweg-DOC model* in which the DOC transects were predicted from environmental monitoring data (Table S1) including river discharge, WL, and a remotely sensed marsh enhanced vegetation index 2 (EVI2). Finally, the *thalweg-DOC model* was implemented between 2017 and 2023, and validated against in situ measurements of DOC concentration collected within 200 m of the PIE thalweg.

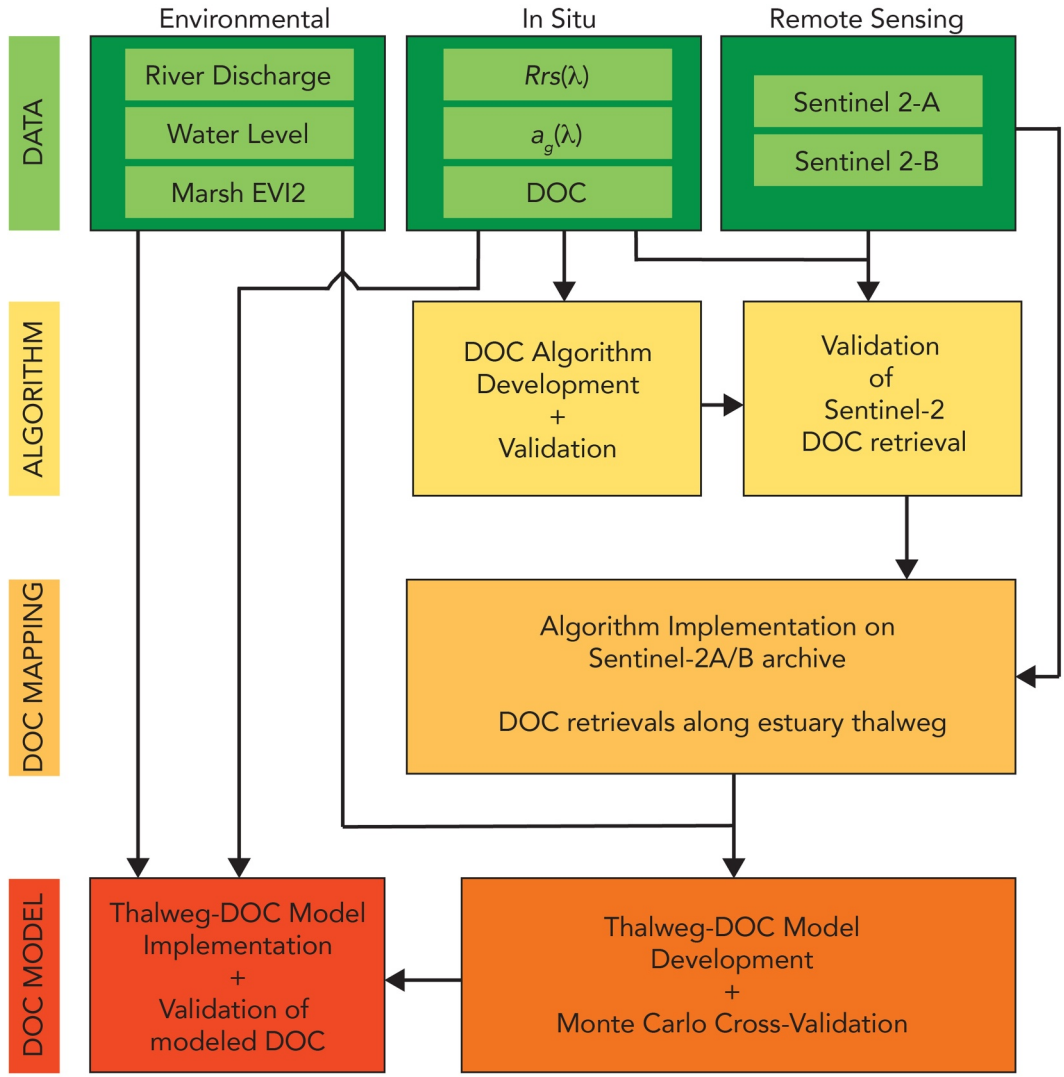

Figure 3. Flowchart summarizing the overall methodology used to develop and validate the thalweg-DOC model at the Plum Island Estuary (PIE). In situ measurements of $R_{rs}(\lambda)$, CDOM absorption coefficient, and dissolved organic carbon (DOC) concentration were collected and used to develop and independently validate (leave-one-out validation, and end-to-end validation on Sentinel-2 imagery) a remote-sensing algorithm to retrieve DOC concentration in the PIE. The algorithm used the $R_{rs}(490)/R_{rs}(665)$ band ratio as a predictor in a double exponential model of $a_g(250)$, followed by a second-order polynomial equation to estimate DOC from $a_g(250)$. The algorithm was then implemented on the Sentinel-2 imagery record (>100 clear-sky and glint-free images between 2017 and 2023) to retrieve full transects of DOC concentration along the thalweg of the PIE (see Figure 1c). A multiple linear regression model to predict the DOC transects from 3 predictors (river discharge, water level relative to mean sea level, the 2-band enhanced vegetation index (enhanced vegetation index 2) averaged over the PIE marsh area) was then developed, validated using a Monte Carlo cross validation, and implemented for a 15-min time-step for three entire years spanning 1 January 2020 until 31 December 2022. Finally, the thalweg-DOC model was validated using an independent set of in situ measurements of DOC concentration collected within 200 m of the thalweg from 2017 to 2023.

3.3.2. DOC Algorithm Development and Validation

Simultaneous in situ measurements of $R_{rs}(\lambda)$, CDOM absorption coefficient, and DOC concentrations were used to develop and validate a two-step, local DOC algorithm applicable to Sentinel-2 imagery. In the first step, the algorithm estimates the absorption coefficient of CDOM at 250 nm, $a_g(250)$, from the $R_{rs}(490)/R_{rs}(665)$ band ratio using a double exponential fit. In the second step, the algorithm retrieves DOC concentration from $a_g(250)$ using a quadratic fit. The data set used was divided into independent training and validation subsets, allocating 88% of the stations for training and the remaining 12% for validation. The 88-% training subset encompassed most

of the in situ data because it was used to derive the fitting coefficients of the double exponential and quadratic fits used in the two sequential steps of the algorithm, and it was used in a leave-one-out validation to assess the robustness of the approach. The 12-% validation subset was used to test the performance of the final algorithm when implemented on an independent data set, and was specifically selected to correspond to the data collected during the 6 coincident Sentinel-2 overpasses used for validating the Sentinel-2 DOC retrievals (see Section 3.3.3).

3.3.3. Validation of Sentinel-2 DOC Retrieval

The accuracies of the satellite-derived $R_{rs}(\lambda)$, $a_g(250)$, and DOC were determined using a match-up analysis between in situ and satellite data. Co-located and simultaneous (within ±1.5 hr) in situ measurements were collected during 6 different clear-sky Sentinel-2 overpasses (1 October 2020, 9 October 2020, 14 October 2021, 6 October 2022, 19 October 2022, and 19 May 2023). The Sentinel-2 images were downloaded from the CNES PEPS website (https://peps.cnes.fr) (CNES, n.d.) and were atmospherically corrected using the ACOLITE software with the Dark-Spectrum Fitting method (Vanhellemont, 2019; OD Nature, n.d.) to produce maps of $R_{rs}(\lambda)$ at the Sentinel-2 bands centered at 443, 490, 560, 665, and 705 nm. The DOC-algorithm was then implemented on the Sentinel-2 $R_{rs}(\lambda)$ to retrieve maps of $a_g(250)$ and DOC concentrations. The satellite-derived $R_{rs}(\lambda)$, $a_g(250)$ and DOC concentration were then compared to their matched-up in situ equivalents, and the satellite retrieval accuracy was assessed using the residual mean square error (RMSE), the mean absolute percent error (MAPE), and the coefficient of determination of the linear fit.

3.3.4. Compilation of Environmental Monitoring Variables

Three environmental monitoring variables were used as predictors of DOC concentration in the *thalweg-DOC model*: (a) The Parker River discharge, (b) the WL relative to mean-sea-level in the Plum Island Sound, and (c) the EVI2 vegetation index over the PIE marsh. The Parker River discharge data for the time period of interest (4 July 2017–4 September 2023) was obtained from the USGS site 01101000 in Byfield, MA, where discharge was measured every 15 min (https://waterdata.usgs.gov/nwis/uv?site_no=01101000) (USGS, n.d.). Water level (mean sea level datum) at a 15-min interval was obtained from the NOAA Tide Predictions database for the Plum Island South station 8441241 (https://tidesandcurrents.noaa.gov/stationhome.html?id=8441241) (NOAA, n.d.). The derivative of WL data was used to estimate the rate of WL change at a 15-min interval. Finally, the Enhanced Vegetation Index (EVI)-2 was calculated as in Equation 4 (Jiang et al., 2008) and averaged over the extent of the PIE marsh area as a proxy for marsh vegetation phenology:

$$\mathrm{EVI2} = \frac{2.5 * (NIR - \mathrm{Red})}{NIR + 2.4 * \mathrm{Red} + 1} \tag{4}$$

where *NIR* refers to the surface reflectance at the Sentinel-2 near-infrared band centered at 842 nm, and Red refers to the surface reflectance at the Sentinel-2 red band centered at 665 nm. The extent of the PIE marsh area (brown area in Figure 1) was obtained from the National Wetland Inventory (USGS, 2023). The EVI2 was then interpolated to a 15-min interval using a spline function as in Bolton et al. (2020).

3.3.5. DOC Mapping Using the Sentinel-2 Archive, and Extractions of DOC Along the Thalweg

The tandem of Sentinel-2A/B sensors have a combined revisit time of 5 days, together providing >400 images collected over the PIE during the study period (4 July 2017–4 September 2023). However, sun glint during the summer months, cloud cover, and/or challenging atmospheric conditions (e.g., wildfire smoke) considerably limited the number of useable images (ESA, 2015). Overall, a total of 141 clear-sky and Sentinel-2 images with minimal sun glint were considered useable for the analysis and were downloaded from the CNES PEPS website (https://peps.cnes.fr) (CNES, n.d.). Atmospherically corrected Sentinel-2 $R_{rs}(\lambda)$ images (Vanhellemont, 2019) were used to generate thematic maps of DOC concentrations in the PIE. DOC concentrations were retrieved over areas of the estuary where bottom reflectance was considered negligible, and the shallow areas influenced by bottom reflectance were masked. The remotely sensed DOC concentrations along the ∼17-km-long estuary thalweg transect (shown Figure 1c) were then extracted from each of the 141 Sentinel-2 scenes. These are referred to as "thalweg-DOC transects" in this manuscript. All DOC maps shown in this manuscript were generated using the Generic Mapping Tools software (Wessel et al., 2019; GMT, n.d.).

Table 2
Coefficients of Thalweg-DOC Model Developed in This Study (Equations 6 and 7)

	Intercept	Intercept std deviation	Q	Q std deviation	WL	WL std deviation	EVI2	EVI2 std deviation
α	a		b		c		d	
	601.202	10.808	1.782	0.104	−112.803	3.244	−657.636	36.510
β	e		f		g		h	
	−0.119	0.002	-9.157×10^{-7}	1.360×10^{-5}	0.005	6.167×10^{-4}	0.139	0.006

3.3.6. Thalweg-DOC Model Development and Validation

The *thalweg-DOC model* was developed to estimate the thalweg-DOC concentration transects from three simple environmental predictors: (a) Parker River discharge, (b) WL, and (c) EVI2. In order to simplify the modeling and avoid overfitting, each thalweg-DOC transect was first approximated using a 2-parameter exponential fit, as shown in Equation 5:

$$DOC_{\text{thalweg}} = \alpha * \exp(\beta * D_{\text{thalweg}}) \quad (5)$$

where DOC_{thalweg} refers to the DOC concentrations along the thalweg [μmol L^{-1}], D_{thalweg} is the distance along the thalweg [km], and α and β are the coefficients derived from the non-linear fit. A multiple linear regression (MLR) was then used to predict α and β from the three environmental predictors, as summarized in Equations 6–7:

$$\alpha = a + b * Q + c * WL + d * EVI2 \quad (6)$$

$$\beta = e + f * Q + g * WL + h * EVI2 \quad (7)$$

where Q is the Parker River discharge [$ft^3\ s^{-1}$], WL is the WL relative to mean sea level [m], EVI2 is the average EVI2 calculated for the PIE marsh area, and a, b, c, d, and e, f, g, h are the regression coefficients of the MLR corresponding to α and β, respectively. The values corresponding to these coefficients are provided in Table 2.

Monte Carlo cross validation procedure was used to assess the ability of the MLR model to retrieve the DOC concentrations transects accurately. For this procedure, the data set of 141 Sentinel-2 derived thalweg-DOC transects was divided into a training subset ($n = 132$) and a validation subset ($n = 9$), allowing the MLR parameters determined using the training subset to be independently tested with the validation subset. Specifically, the performance of the MLR models was assessed by calculating the R^2, RMSE, MAPE between the remotely sensed thalweg DOC concentrations and those derived from the *thalweg-DOC model*. An initial validation subset was manually selected to provide a representative range and combination of environmental conditions (e.g., high and low tide, ebb and flood tide, high and low river discharge, and low and high EVI values), and was used to illustrate the performance assessment in the figures of this manuscript. However, this process was repeated an additional 30 times, each time using a different and random combination of 132 transects for training and 9 transects for validation. The overall performance and combined statistics from the 31 cross-validations were compiled and are reported. The final *thalweg-DOC model* was trained using all 141 transects.

To evaluate its performance during extreme conditions of WL and discharge, the *thalweg-DOC model* was also trained using 129 transects and independently tested on the 12 most "extreme" transects of this data set (e.g., transects associated with the 3 highest and lowest river discharges, and the 3 highest and lowest water levels of the observation period), and the same performance metrics (e.g., R^2, RMSE, MAPE) were compared. Finally, the final *thalweg-DOC model* was implemented using extreme values of river discharge and WL that were beyond the range of those used to train the model (river discharge from 170 to 210 $ft^3\ s^{-1}$ by increments of 10 $ft^3\ s^{-1}$, and WL ranging from −1.8 to −2.2 m and 1.8–2.2 m by increments of 0.1 m) to assess if the modeled DOC concentrations remained realistic and conformed to expectations.

3.3.7. Thalweg-DOC Model End-To-End Validation

The performance of the *thalweg DOC model* was also tested by comparing predicted DOC concentrations to in situ DOC concentrations measured at all stations located within 200 m of the thalweg visited during the 2017–

2023 sampling period ($n = 75$). This validation data set was entirely independent from the *thalweg-DOC model* development considering these were stations where no $R_{rs}(\lambda)$ were available and were therefore not used in the algorithm development and validation. Most of this validation data was collected in 2018 and 2022.

3.3.8. Thalweg-DOC Model Implementation for the 2020–2022 Time Period

The final *thalweg DOC model* was implemented at a 15-min interval over a 3-year period from 1 December 2020 to 31 December 2022, to showcase the inputs and outputs of the models and their relationships over multiple years. The time series were generated for each predictor: discharge, WL, and EVI2. The DOC concentrations were modeled at three distinct locations along the thalweg transect (Figure 1d): upstream (Stn1), mid-estuary (Stn2), and downstream (Stn3).

4. Results and Discussion

4.1. The PIE: A CDOM-Dominated System

The PIE was characterized by a large gradient of DOC concentrations across the freshwater-marine continuum, and by low-to-moderately turbid waters with moderate plankton biomass (Figures S3–S4 in Supporting Information S3 and Table 1). The data collected for this study spanned a salinity range of 0–32 (median of 22) and a corresponding DOC-concentration range of 90–900 μmol L^{-1}, with the two variables being strongly inversely correlated (Figure S3a in Supporting Information S3; $R = -0.82$), as is typically observed in estuaries (Del Vecchio & Blough, 2004; Fichot & Benner, 2012; Juhls et al., 2019). The turbidity ranged from <0.5 to 10 FNU, corresponding to a TSS concentration range of about 1–20 mg L^{-1} (Figure S4 in Supporting Information S3), with a median of 3 FNU (TSS ~5–6 mg L^{-1}). The chlorophyll-a fluorescence was also moderate (typically <2 RFU), corresponding roughly to chlorophyll-a concentrations <8–10 μg L^{-1}. As indicated by the positive relationships between DOC and chlorophyll-a fluorescence (Figure S3b in Supporting Information S3; $R = 0.52$) or turbidity (Figure S3c in Supporting Information S3; $R = 0.70$), suspended particle concentration was generally higher in the upper reaches of the estuary, consistent with rivers and saltmarshes contributing sediments and nutrients to narrow channels (Fagherazzi et al., 2014; Harringmeyer et al., 2024; Hopkinson et al., 2018). Overall, suspended particle concentrations in this system were low relative to the wide range of DOC concentrations.

The optical properties of the PIE waters were dominated by variability in the CDOM absorption coefficient, which represented a strong proxy for DOC concentration in these waters. DOC concentration was strongly and positively correlated with the CDOM absorption coefficient across the full range of observed DOC concentrations (Figure S3d in Supporting Information S3). This indicated CDOM is an excellent optical proxy for DOC concentration in the PIE, consistent with similar observations in other estuarine systems (Cao et al., 2018; Fichot & Benner, 2011; Mannino et al., 2008). Very strong relationships between the CDOM absorption coefficient, $a_g(\lambda)$, and the diffuse attenuation coefficient $K_d(\lambda)$ at $\lambda = 340$, 412 and 490 nm ($R^2 = 0.99$, 0.97, and 0.90, respectively) also demonstrated that CDOM is the dominant driver of vertical light attenuation in this system (Figures S5a–S5c in Supporting Information S3). A comparison of the absorption coefficient of CDOM, non-algal particles, $a_d(\lambda)$, and algal particles, $a_{ph}(\lambda)$, further showed that CDOM dominated the total absorption coefficient of the water in the UV and blue spectral range (Figures S5d–S5f in Supporting Information S3). The slopes of the linear regressions of $K_d(\lambda)$ on $a_g(\lambda)$ were 1.21, 1.31 and 1.58 at $\lambda = 340$, 412 and 490 nm, respectively, further confirming CDOM is the main contributor to $K_d(\lambda)$.

4.2. Development and Validation of DOC Algorithm for Sentinel-2 MSI

The optical dominance of CDOM in the PIE facilitated the development of a simple but robust band-ratio algorithm to retrieve $a_g(\lambda)$ from remote-sensing reflectance (Figure S6 in Supporting Information S3 and Figure 4). A cursory assessment first revealed that increasing DOC concentrations led to a decrease of $R_{rs}(\lambda)$ in the blue region relative to the red, a pattern evident from both the C-OPS (Figure S6a in Supporting Information S3) and the PSR-1100f (Figure S6b in Supporting Information S3) measurements and in line with the expected effect of increasing CDOM absorption on reflectance (Fichot et al., 2023). The observation of an exponential relationship between $a_g(250)$ and $R_{rs}(490)/R_{rs}(665)$, as used in previous studies (Keith et al., 2016; Mabit et al., 2022), allowed for the quantification of this effect (Figure 4a). Specifically, a double exponential regression of $a_g(250)$ on $R_{rs}(490)/R_{rs}(665)$ yielded an R^2 value of 0.96, and a corresponding leave-one-out validation indicated this algorithm predicted $a_g(250)$ within ±20.3% (RMSE of 4.41 m^{-1}) of the laboratory measurement (Figure 4b).

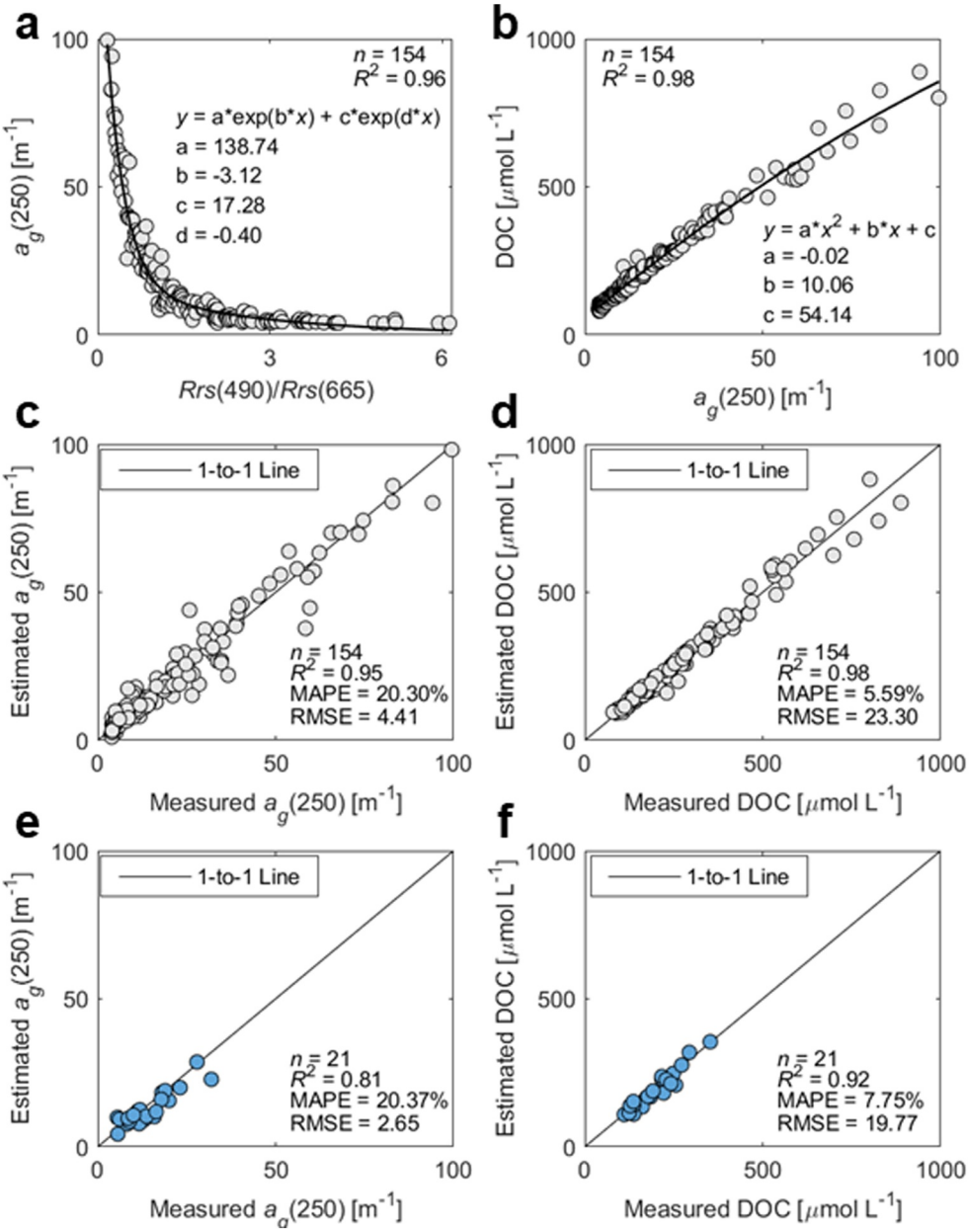

Figure 4. Development and validation of the two steps making up the dissolved organic carbon (DOC) algorithm. (a) Relationship between $R_{rs}(490)/R_{rs}(665)$ and $a_g(250)$ in the training data set and corresponding double-exponential fit and regression coefficients used to predict $a_g(250)$ from $R_{rs}(490)/R_{rs}(665)$ in the algorithm. (b) Relationship between $a_g(250)$ and DOC concentration in the training data set, and corresponding quadratic fit and regression coefficients used to predict DOC from $a_g(250)$ in the algorithm. (c) Leave-one-out validation of $a_g(250)$ estimated from $R_{rs}(490)/R_{rs}(665)$ using the double-exponential fit approach applied to the training data set. (d) Leave-one-out validation of the DOC concentration estimated from $a_g(250)$ using the quadratic fit approach applied to the training data set. (e) Independent validation of $a_g(250)$ estimated from $R_{rs}(490)/R_{rs}(665)$ using the double-exponential fit approach applied to the validation data set. (f) Independent validation of the DOC concentration estimated from $a_g(250)$ using the quadratic fit approach applied to the validation data set. The number of observations (n), the coefficient of determination (R^2) of regressions, the mean absolute percent error (MAPE), and the root mean square error (RMSE) are presented in the panels. The in situ data set was separated into two sets: training (comprising 88% of the total data set) and validation (comprising 12% of the total data set). The training data is shown with gray points, while the validation data is depicted with blue points.

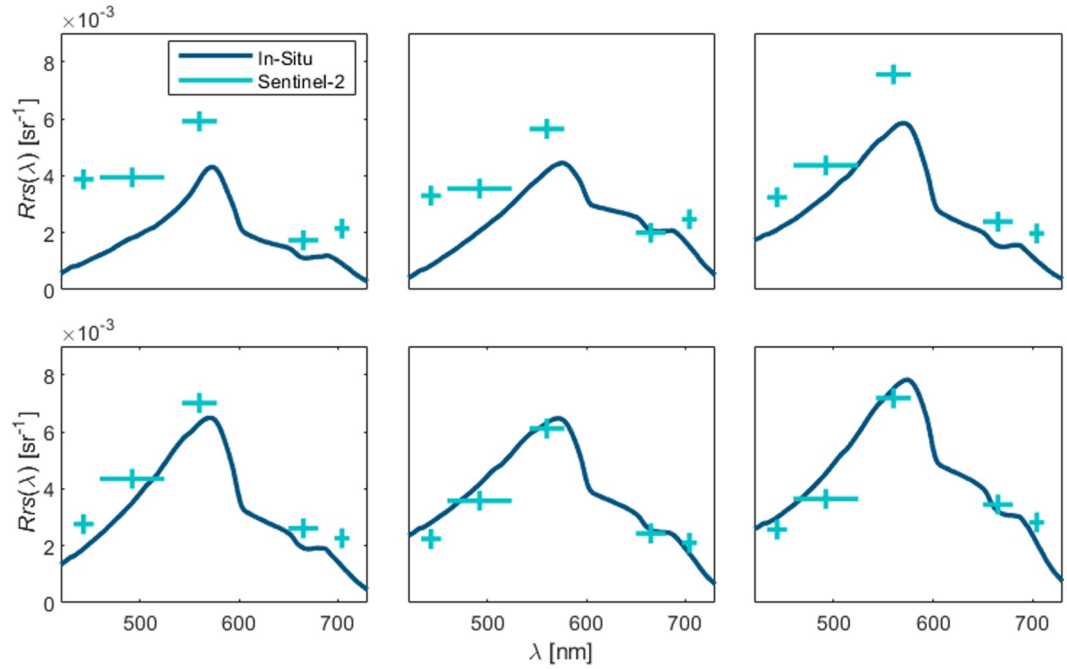

Figure 5. Comparison of $R_{rs}(\lambda)$ spectra derived from Sentinel-2 and from in situ measurements collected with the above-water approach (PSR-1100f) for a representative set of six matched-up stations (selected among a total of $n = 21$; complete set shown in Figure S9 in Supporting Information S3). The in situ hyperspectral $R_{rs}(\lambda)$ measured with the PSR-1100f are depicted by continuous dark-blue lines. The Sentinel-2 multispectral $Rrs(\lambda)$ in the visible range (derived using ACOLITE) are represented by discrete light-blue crosses, with the vertical line showing the center of the Sentinel-2 wavebands (443, 490, 560, 665, and 705 nm) and the light-blue horizontal lines corresponding to the width of the band.

Additional test using the in situ validation data set confirmed a similar level of uncertainty (MAPE of±20.3% and RMSE of 2.65 m^{-1}) when the algorithm was implemented on that independent data set (Figure 4c).

The absorption coefficient of CDOM proved a very robust proxy of DOC concentration in the PIE, facilitating its indirect estimation from remote sensing (Figure 4 and Figure S7 in Supporting Information S3). A strong but slightly curvilinear relationship between DOC concentration and $a_g(\lambda)$ was observed across the 250–450 nm spectral range (Figure S7 in Supporting Information S3). This relationship was strongest for $a_g(250)$ and slightly weaker for $a_g(450)$. Therefore, $a_g(250)$ was selected as the predicted variable in the band-ratio algorithm. A quadratic fit of DOC on $a_g(250)$ achieved an R^2 of 0.98 (Figure 4b) and a corresponding leave-one-out validation indicated DOC concentration could be estimated from $a_g(250)$ within ±5.5% (RMSE of 23.3 μmol L^{-1}) of the laboratory measurement (Figure 4d). Additional validation using the in situ validation data set confirmed a similar level of uncertainty (MAPE of ±7.7%; RMSE of 19.7 m^{-1}) when the model was implemented on that independent data set (Figure 4f). The spectral slope coefficient between 275 and 295 nm, $S_{275–295}$, has previously been used as an additional predictor to improve estimates of DOC concentration from $a_g(\lambda)$ in several estuaries and coastal water bodies (Araújo & Bélanger, 2022; Cao et al., 2018; Fichot & Benner, 2011). However, the use of this additional parameter had only very minor effects on the predictability of DOC in this system, and was not warranted. Its use would unnecessarily increase the complexity of the approach and likely introduce additional uncertainty in DOC retrievals considering $S_{275\text{-}295}$ would also have to be retrieved accurately from remote sensing (Cao et al., 2018; Fichot et al., 2014).

4.3. End-To-End Validation of Sentinel-2 Retrievals

Validation of the Sentinel-2 $R_{rs}(\lambda)$ against matched-up in situ measurements revealed reasonably accurate atmospheric correction in the visible range and resulting $R_{rs}(490)/R_{rs}(665)$ retrievals (Figures 5 and 6). After a thorough tuning of parameters to optimize performance, the set of 21 matched-up $R_{rs}(\lambda)$ spectra revealed the atmospheric correction produced $R_{rs}(\lambda)$ with comparable spectral shapes and magnitudes as the in situ measurements (Figure 5 and Figure S8 in Supporting Information S3). A comparison in the visible region ($\lambda = 443$,

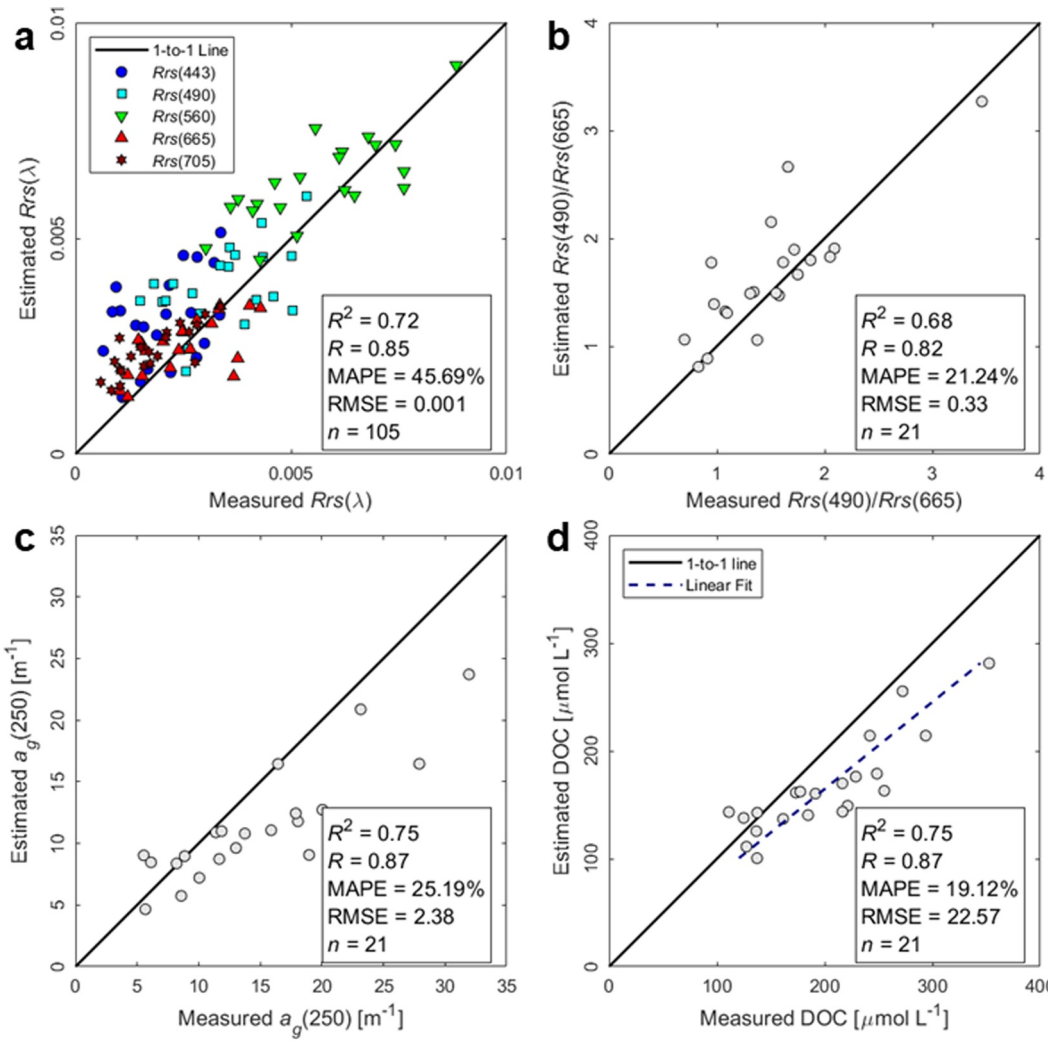

Figure 6. Accuracy assessment of $R_{rs}(\lambda)$, $a_g(250)$, and dissolved organic carbon (DOC) retrieved from Sentinel-2 imagery and matched up with corresponding in situ measurements collected along the Plum Island Estuary thalweg. (a) Sentinel-2 (Estimated) versus in situ (Measured) $R_{rs}(\lambda)$ for five Sentinel-2 wavebands in the visible range (443, 490, 560, 665, and 705 nm). (b) Sentinel-2 (Estimated) versus in situ (Measured) $R_{rs}(490)/R_{rs}(665)$ band ratio. (c) Sentinel-2 (Estimated) versus in situ (Measured) CDOM absorption coefficient at 250 nm, $a_g(250)$. (d) Sentinel-2 (Estimated) versus in situ (Measured) DOC concentration. Sentinel-2-derived DOC concentrations were biased overestimating the field measurements. In order to maximize accuracy of the DOC retrievals, a linear regression of the Measured DOC on the Estimated DOC was performed, and the fit was used in a post-processing step to remove the bias. The linear fit is shown here as a dashed dark blue line. The coefficient of determination (R^2), the correlation coefficient (R), the Mean Absolute Percentage Error (MAPE), the Root Mean Square Error (RMSE) are shown in all panels here as measures of performance.

490, 560, 665, 705 nm) showed good correlation ($R = 0.84$) and reasonable uncertainty (MAPE ± 45%) in the Sentinel-2 $R_{rs}(\lambda)$ relative to their in situ equivalent, but also revealed a systematic bias toward overestimation by Sentinel-2 (Figure 6). The most prominent mode of error was a significant offset in the overall magnitude of the spectrum, but in most cases the spectral shape of the Sentinel-2 $R_{rs}(\lambda)$ was relatively well preserved in the red and blue regions. Here, the use of $R_{rs}(490)/R_{rs}(665)$ as a single predictor was therefore advantageous because a band ratio was less sensitive to offsets. The time difference between Sentinel-2 overpasses and in situ measurements could have contributed to the observed differences. A narrow window of ±1.5 hr from the overpass was used to ensure there were multiple match-up available for each Sentinel-2 scene. However, even a 1.5-hr difference can lead to significant differences in optical conditions in a mesotidal system like the PIE. This is accentuated up-stream, where the salinity gradient can occur over a short distance, and during mid-tide when conditions are

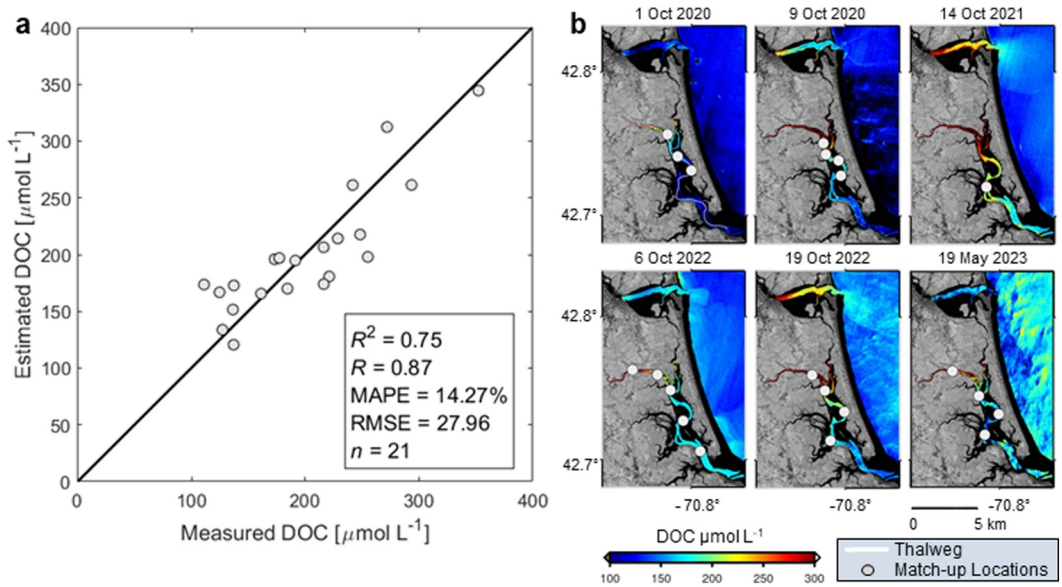

Figure 7. Validation of post-processed Sentinel-2 dissolved organic carbon (DOC) retrievals, along with corresponding DOC maps and match-up locations along the thalweg of the Plum Island Estuary (PIE). (a) Sentinel-2 (Estimated) versus in situ (Measured) DOC concentrations. The coefficient of determination (R^2), the correlation coefficient (R), the Mean Absolute Percentage Error (MAPE), the Root Mean Square Error (RMSE) are shown as measures of performance. (b) DOC concentration maps of the PIE derived using the local algorithm (after post-processing) for the six match-up dates: 1 October 2020, 9 October 2020, 14 October 2021, 6 October 2022, 19 October 2022, and 19 May 2023. The locations of the matched-up measurements are shown as gray points. The thalweg of the estuary is shown in the Sentinel-2 image acquired on 1 October 2020.

changing rapidly. The tidal conditions for each match-up are summarized in the (Figure S9 in Supporting Information S3).

Validation of the remotely sensed $a_g(250)$ and DOC showed the algorithm effectively captured the range and variability of the in situ measurements, but also revealed a systematic and significant bias in the retrievals that warranted a post-processing correction (Figures 6c, 6d and 7). The Sentinel-2 $a_g(250)$ and DOC correlated well (R = 0.87) with the corresponding in situ measurements, and approximated them within ±25 and ±19%, respectively. However, a systematic underestimation by 20%–25% of both products was also evident and was partly caused by the residual bias in $R_{rs}(490)/R_{rs}(665)$. A linear regression of the in situ (Measured) DOC on the Sentinel-2 (Estimated) DOC (Figure 6d) proved an effective approach to rectify this systematic underestimation, and led to improved and unbiased DOC retrievals that were within <15% of the in situ measurements (Figure 7a). This level of accuracy was comparable to that attained in previous remote sensing studies of estuarine DOC (Cao & Tzortziou, 2021; ChunHock et al., 2020; Signorini et al., 2019). This linear fit ($y = 1.239 \times x - 4.057$) was therefore used as a post-processing step in the algorithm to avoid the propagation of this systematic bias, and was applied to all Sentinel-2 images. This final DOC algorithm produced realistic DOC maps for the PIE (Figure 7b). These maps showed high DOC concentrations upstream that decreased progressively toward the ocean, and were within the range expected in this system (Raymond & Hopkinson, 2003; Uhlenhopp et al., 1995). This end-to-end validation provided confidence in the quality of the Sentinel-2 retrievals before implementation on the Sentinel-2 image archive.

4.4. Implementation of the DOC Algorithm on the Sentinel-2 Archive

The assembled archive of Sentinel-2 images generated a time series that was representative of most environmental conditions encountered in the PIE (Figure 8). A total of 141 useable scenes were gathered over a period of >6 years, meaning a useable Sentinel-2 scene was available every 16 days on average. This archive was able to capture representative ranges of the Parker River discharge (0–200 $ft^3\ s^{-1}$; Figure 8a), marsh EVI2 (0.1–0.4; Figure 8b), and tidal stage characterized by WL (range of −1.7 to 1.7 m; Figure 8c) and rate of WL change (range of −0.8 to 0.8 $m\ hr^{-1}$; Figure 8d). Importantly, the time series was long enough to encompass many combinations

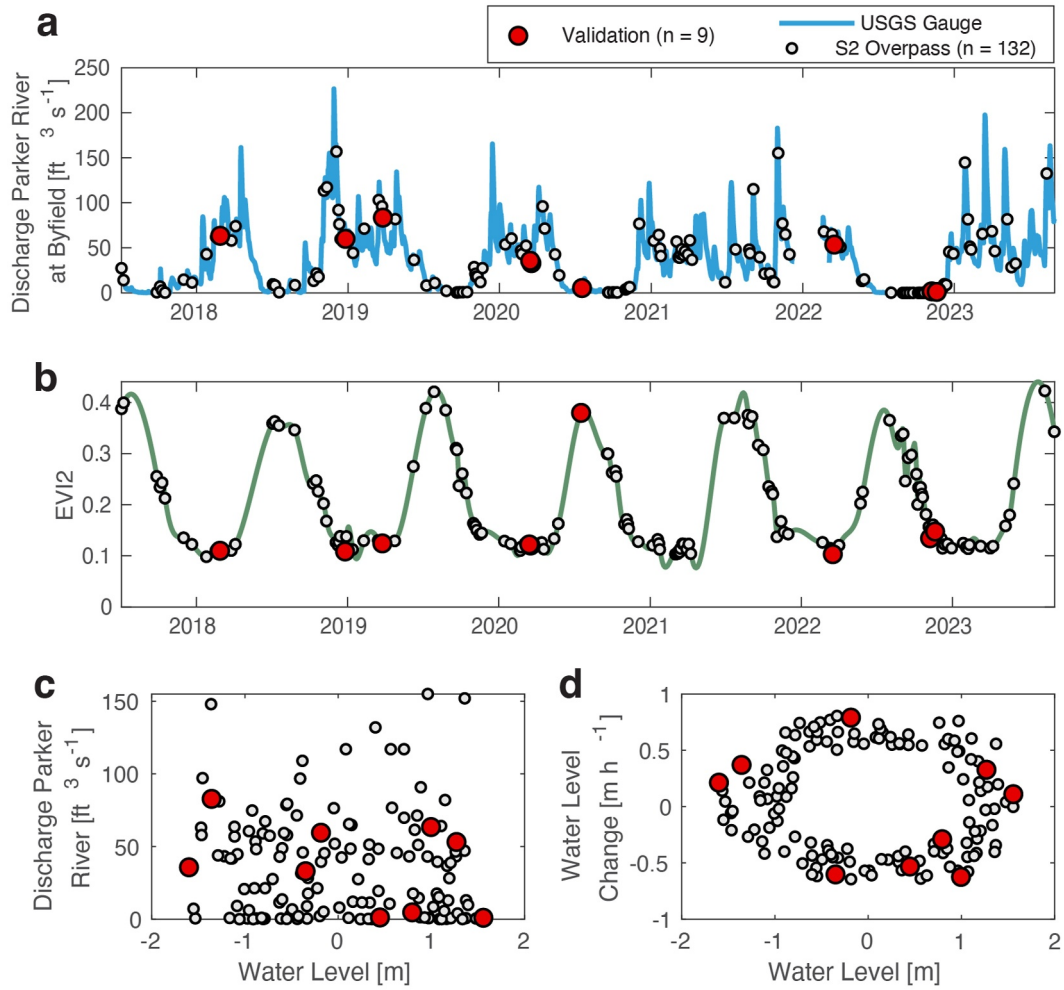

Figure 8. Overview of the hydrological, marsh biomass indicator, and tidal conditions corresponding to the Sentinel-2 image archive used to develop the Plum Island Estuary (PIE) *thalweg-DOC model*. (a) Parker River discharge measured at the USGS Byfield station in Massachusetts, and corresponding Sentinel-2 scenes used in the thalweg-DOC model. (b) Sentinel-2 Enhanced vegetation index (enhanced vegetation index 2) averaged over the saltmarsh area of the PIE (see Figure 1b) and interpolated using a spline function and corresponding Sentinel-2 images used in the thalweg-DOC model. (c) Parker River discharge measured at the USGS Byfield station in Massachusetts versus water level (WL) (relative to mean sea level) at the Plum Island Sound, corresponding to the Sentinel-2 images used in the thalweg-DOC model. (d) Rate of WL change versus WL (relative to mean sea level) at the Plum Island Sound, corresponding to the Sentinel-2 images used in the thalweg-DOC model. Red points represent the Sentinel-2 images used in the validation of the *thalweg-DOC model* (see Figures 9 and 12). Gray points represent all other Sentinel-2 images used to develop the *thalweg-DOC model*.

of these environmental conditions, which operate on different time scales (e.g., days/weeks for discharge, weeks/months for EVI2, and hours for tidal stage). The archive also covered all seasons, although more scenes were typically available in the spring and fall compared to other seasons (Figure S10 in Supporting Information S3). In particular, fewer scenes were available in early summer (e.g., very few in June) due to sun glint contamination (Fell, 2022; Harmel et al., 2018), and several scenes were partially impacted by sea ice in winter (January/February typically). Unfortunately, the impacts of large storms, which are often associated with enhanced DOC fluxes and cycling (Avery et al., 2004; Bianchi et al., 2013; Osburn et al., 2019; Yan et al., 2020), were not well represented in this archive because such episodic events are difficult to capture with the current revisit times of HSRRS satellites and heavy cloud cover is typically associated with these weather events.

Implementation of the algorithm on the Sentinel-2 archive generated a collection of realistic DOC-concentration maps suitable for the analysis of DOC dynamics in the PIE (Figure 9 and Catalog in Supporting Information S2). Nine representative scenes (Figure 9) captured the range in DOC distributions, demonstrating that variability in

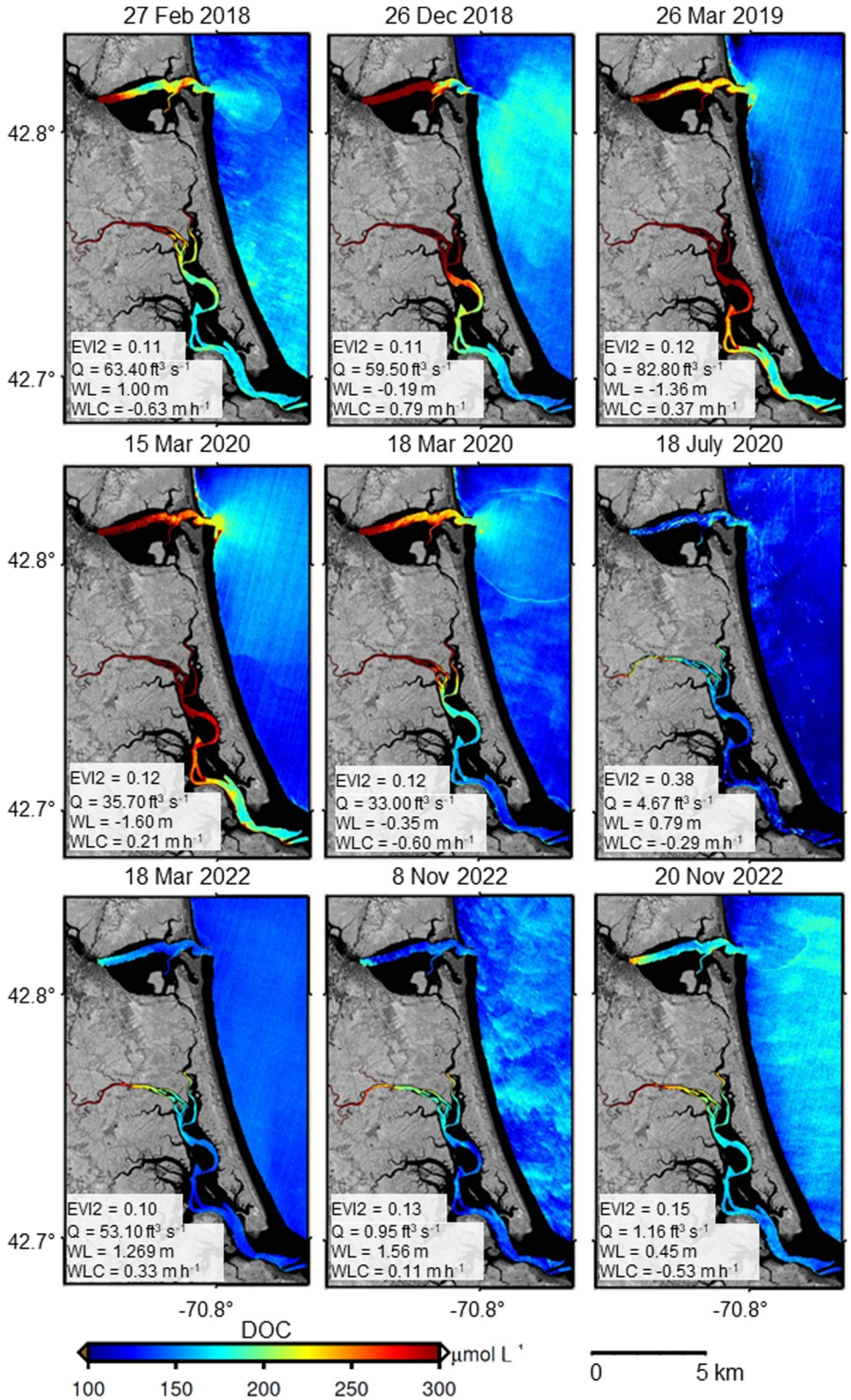

Figure 9.

remotely sensed DOC followed expected patterns of higher concentration upstream, at low tide, and during elevated river discharge. The highest concentrations were observed when these conditions overlapped. A comparison of two scenes collected only three days apart (15 March 2020 and 18 March 2020) clearly illustrated the effects of tidal stage on DOC concentrations. In that instance, high DOC waters (250–300 μmol L^{-1}) observed at low tide (WL = −1.60 m) on 15 March were evidently diluted by lower-DOC (~100 μmol L^{-1}) marine waters on March 18th, when WL was higher (WL = −0.37 m) and the tide was ebbing. Although the archive was not able to represent the effects of specific episodic events, it captured a wide range of extreme conditions. For instance, an extremely low DOC gradient along the estuary (100–200 μmol L^{-1}) was captured on 9 September 2022, during a combination of peak high tide and extremely low discharge associated with a regional drought (Catalog in Supporting Information S2). In a contrasted example, an extremely steep DOC gradient along the estuary (200–1,000 μmol L^{-1}) was observed on 25 April 2019, during low-tide conditions and following a major snowmelt event in Massachusetts (Catalog in Supporting Information S2). This representative collection of Sentinel-2 DOC maps was sufficiently large and of sufficient quality to investigate the interplay of drivers on the complex DOC dynamics of this tidal marsh-influenced estuary.

4.5. Drivers of DOC Variability in the PIE

River discharge and WL both had a major influence on the DOC concentrations of this tidal estuary (Figure 10 and Figure S11 in Supporting Information S3), in line with similar observations made in the largest marsh system of Chesapeake Bay (Cao & Tzortziou, 2021). The remotely sensed DOC concentrations along the PIE thalweg increased with river discharge (R^2 = 0.28), particularly as discharge increased from low to moderately high (Figures 10a and 10d). High river discharge can contribute to higher estuarine DOC concentrations in multiple ways. First, high discharge is often associated with high DOC concentration in temperate and high-latitude rivers (Cai et al., 2015; Pérez-Rodríguez & Biester, 2022; Zarnetske et al., 2018). This relationship often exists in these systems because discharge typically peaks in the spring (driven by snowmelt and higher rainfall) flushing topsoils enriched with fresh organic matter from the fall litter decomposition (Raymond & Saiers, 2010), and this spring flushing is typically followed by a summer period of decreased discharge draining already flushed-out soils. Second, higher river discharge increases the fraction of relatively high-DOC freshwater within the estuary, displacing saline, low-DOC seawater. Finally, higher discharge can decrease freshwater residence time in the estuary, reducing the extent of DOC mineralization occurring in the estuary. The Sentinel-2 DOC concentrations were also strongly (R^2 = 0.35) and inversely related to the WL, confirming this factor is a dominant driver of DOC variability in the PIE (Figures 10b and 10e). Tidally driven oscillations of DOC are generally observed in tidal estuaries (Clark et al., 2018; Menendez et al., 2022; Schiebel et al., 2018), and result primarily from the dilution of terrigenous inputs by relatively low-DOC coastal waters when the tide rises. No relationship was observed between DOC concentrations and the rate of WL change.

A weak negative relationship between marsh EVI2 and DOC concentrations was also observed, although the relationship was complex (Figures 10c and 10f). Higher DOC concentrations were observed during periods of relatively low and rapidly changing EVI2 (0.15–0.2), which generally corresponded to periods of marsh vegetation growth in the spring or senescence in the fall. DOC concentrations were generally lower during periods of high EVI2 (0.3–0.4), which generally corresponded to periods of peak marsh biomass during summer. This observation differs from previous reports that DOC concentrations in wetland-estuarine systems are consistently higher during periods of high biomass in summer and early fall (Cao & Tzortziou, 2021; Tzortziou et al., 2008). This difference is likely caused by a much greater influence of riverine inputs in the PIE, which skews peak DOC concentration earlier in the spring when the DOC flux from the rivers is highest. This difference might also arise because the PIE is largely dominated by high marsh, which only gets significantly flooded around spring tides (Forbrich et al., 2018; Hopkinson et al., 2018), and possibly receives fewer marsh inputs than systems dominated by low marsh. Nonetheless, the EVI2 likely remains indicative of marsh inputs from the fall senescence period

Figure 9. Representative maps of dissolved organic carbon (DOC) concentrations from Sentinel-2 imagery. These specific maps were chosen to showcase DOC concentrations during contrasted environmental conditions. The nine maps correspond to the following dates: 27 February 2018, 4 December 2018, 26 March 2019, 15 March 2020, 18 March 2020, 23 March 2021, 18 March 2022, 8 November 2022, and 20 November 2022. The average marsh enhanced vegetation index 2, the Parker River discharge (*Q*), the water level (*WL*), and the rate of WL change (*WLC*) corresponding to each Sentinel-2 scene is provided in the bottom-left corner of each image. These Sentinel-2 scenes were used for the independent validation of the thalweg-DOC model. A detailed presentation of all 141 scenes and corresponding DOC maps and environmental conditions are provided in a Catalog in Supporting Information S2.

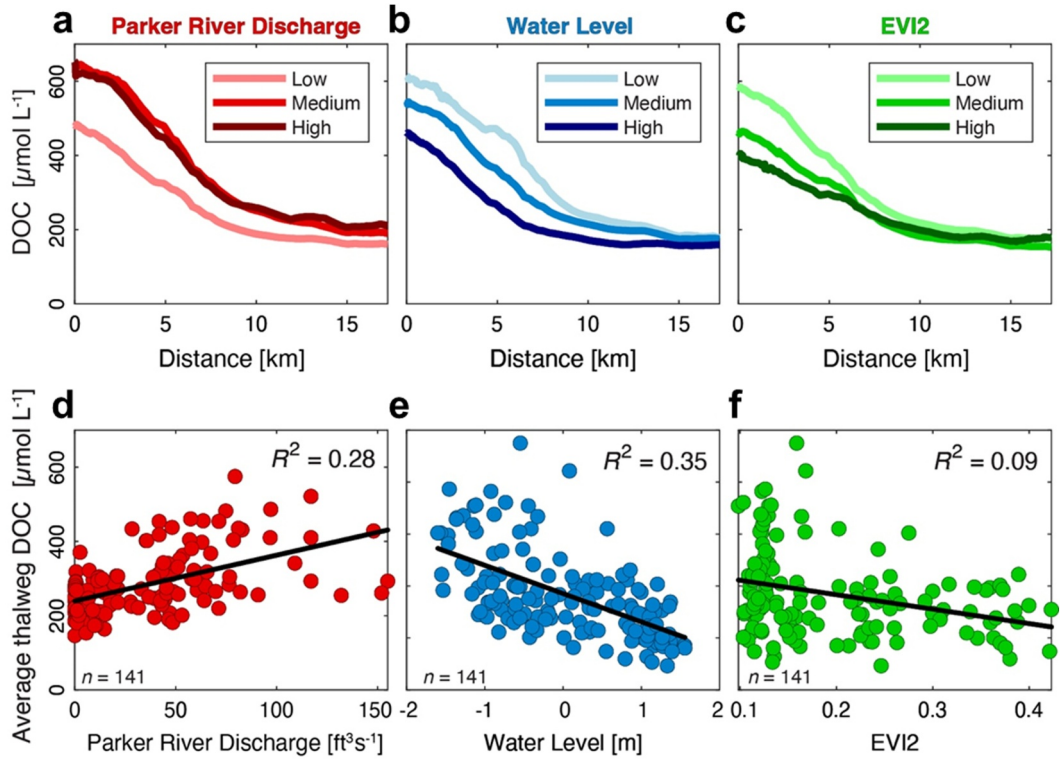

Figure 10. Dependencies of the remotely sensed thalweg dissolved organic carbon (DOC) concentrations on environmental conditions (a–c) DOC-concentration transects derived from Sentinel-2 along the Plum Island Estuary thalweg averaged over three sequential increments (low, medium, high) of Parker River discharge [$ft^3\ s^{-1}$], water level (WL) [m], and marsh enhanced vegetation index 2 (EVI2). The remotely sensed DOC concentrations corresponding to the Parker River discharge, WL, and marsh EVI2 are shown in red (left column), blue (medium column), and green (right column) tones, respectively. The low/medium/high levels for the Parker River discharge corresponds to the (0–51.67)/(51.67–103.33)/(103.33–155.00) $ft^3\ s^{-1}$ ranges, respectively. The low/medium/high levels for the WL corresponds to (−1.60–−0.55)/(−0.55–0.50)/(0.50–1.56) m ranges, respectively. The low/medium/high levels for the EVI2 corresponds to (0.10–0.21)/(0.21–0.31)/(0.31–0.41) ranges, respectively. Corresponding transects with their respective standard deviations are presented Figure S11 in Supporting Information S3. (d–f) Relationships between DOC concentration averaged over the thalweg and the corresponding Parker River discharge, WL, and marsh EVI2 for the $n = 141$ Sentinel-2 scenes of the archive. Each point corresponds to a different scene in the archive. Linear regression fitted line with corresponding coefficient of determination (R^2) are shown.

(Logozzo et al., 2021; Qi et al., 2017; Schiebel et al., 2018; Shelton et al., 2022), when riverine DOC inputs tend to be low in this system (Cronin-Golomb et al., 2022). Here, the marsh EVI2 generally represents an indicator of marsh-input seasonality and was found to have additional predictive ability of DOC concentration in this system.

4.6. Development, Validation, and Implementation of the Thalweg-DOC Model

The Sentinel-2 archive and the analysis of DOC variability informed the development of a simple model capable of predicting the DOC-concentration transect along the PIE thalweg from a few environmental monitoring variables. The individual Sentinel-2 DOC transects decreased exponentially with distance along the thalweg and varied primarily in magnitude and steepness. Despite their adherence to the overall pattern, they often contained subtle variations that were likely the result of interferences/errors. In order to avoid the overparameterization of a model attempting to reproduce this inherent noise, the remotely sensed DOC transects were first fitted using an exponential fit (see Equation 5) that captured the primary features of the transects (Figure 11). This simple 2-parameter (α, β) fit was able to reproduce the magnitude and steepness of the transects while smoothing out potential noise (Figures 11a and 11b). The distribution of exponential-fit R^2 (median of 0.9) corresponding to the 141 scenes indicated that the approach worked well for the vast majority of the transects, with the exception of a few noisy transects (Figure 11c). This simplification facilitated the parameterization of a simple MLR model (*thalweg-DOC model*) in which the parameters α and β were predicted from the Parker River discharge [$ft^3\ s^{-1}$],

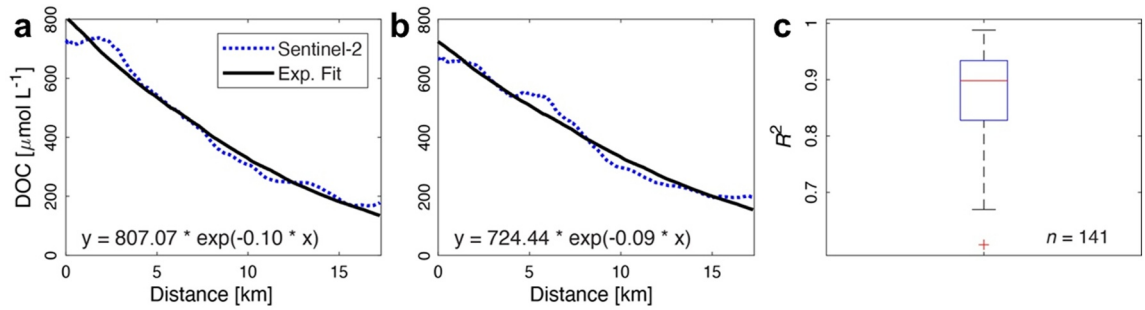

Figure 11. Exponential fitting of remotely sensed thalweg dissolved organic carbon (DOC) transects. (a–b) Two representative examples of the exponential fitting process. The blue lines shows the DOC transects retrieved from Sentinel-2, and the black lines represents the corresponding exponential fits (c) Boxplot showing the distribution of R^2 corresponding to the exponential fits of the 141 remotely sensed DOC transects used in the model development.

WL [m], and marsh EVI2 (Figure S12 in Supporting Information S3). Here, these three variables were used as predictors in the model because they are confirmed drivers of DOC variability in this system (see Section 4.5), and because of their significant predictive capability. In contrast, the rate of WL change was not included as a predictor because it did not have significant predictive capability in this data set. In a first validation step, a total of 132 scenes were used to develop the model, and nine scenes were manually selected for an independent validation.

Validation of the *thalweg-DOC model* using the nine selected validation scenes showed the model reproduced the estuary-wide thalweg DOC distribution reasonably well when implemented on a novel set of images and for a wide range of environmental conditions (Figure 12). The validation scenes (shown in Figure 9) were chosen to cover a representative range of environmental conditions (red points in Figure 8), and supplied a set of remotely sensed DOC transects with very different characteristics (Figure 12a). The modeled DOC transects approximated the shape and magnitude of the exponential fits relatively well, and reproduced the main features of the remotely sensed DOC transects (Figure 12a). A direct comparison of the modeled and remotely sensed DOC returned a median R^2 value of 0.88, a median RMSE of 39 μmol L^{-1}, and a median MAPE of 19.5%, indicating good agreement for these nine transects selected to represent different combinations of environmental conditions. The Monte Carlo cross validation (Figure 12b), which repeated this procedure another 30 times with random permutations of 132 training and 9 validation transects, returned a median R^2 value of 0.88 (range: 0.84–0.92), a median RMSE of 40 μmol L^{-1} (range: 34–46 μmol L^{-1}) and a median MAPE of 23.5% (range: 18%–30%). This validation provided confidence in the ability of the *thalweg-DOC model* to reproduce the main features of DOC transects at the PIE under most environmental conditions.

Specific analyses also showed the *thalweg-DOC model* is expected to perform reasonably well during extreme conditions, such as those associated with storms (Figures S13 and S14 in Supporting Information S3). A cross-validation of the model trained using 129 transects and validated using 12 independent transects with the most extreme water levels and river discharges in our data set (3 highest and 3 lowest water levels, 3 highest and 3 lowest river discharges) returned a median R^2 value of 0.88 (range: 0.80–0.98), a median RMSE of 30 μmol L^{-1} (range: 20.5–72.3 μmol L^{-1}) and a median MAPE of 17.2% (range: 8.7%–44.3%), showing the model still performed relatively well for these extreme conditions (Figure S13 in Supporting Information S3). Furthermore, an implementation using various combinations of river discharge and WL values beyond the range of our data set showed that the final *thalweg-DOC model* produced reasonable DOC estimates that followed expectations for these extreme conditions (Figure S14 in Supporting Information S3). For instance, the model generated higher DOC concentrations for very high river discharge, in line with the frequent observation that the concentrations and fluxes of DOC across estuaries are considerably enhanced during large storms (Bianchi et al., 2013; Hounshell et al., 2019; Medeiros, 2022; Yan et al., 2020). Although these analyses provide some level of confidence about the *thalweg-DOC model*'s performance during extreme conditions, a more thorough and reliable assessment would require the collection of in situ measurements during the entire duration of these large storms (e.g., Nor'easters, Tropical Storms). The acquisition of such validation data sets from boats can be logistically challenging, but it can now be facilitated by the use of tethered in situ water quality sondes equipped with DOM fluorescence sensors, which can now provide increasingly accurate estimates of DOC concentration continuously in these estuarine systems (Menendez et al., 2022; Weiser et al., 2024).

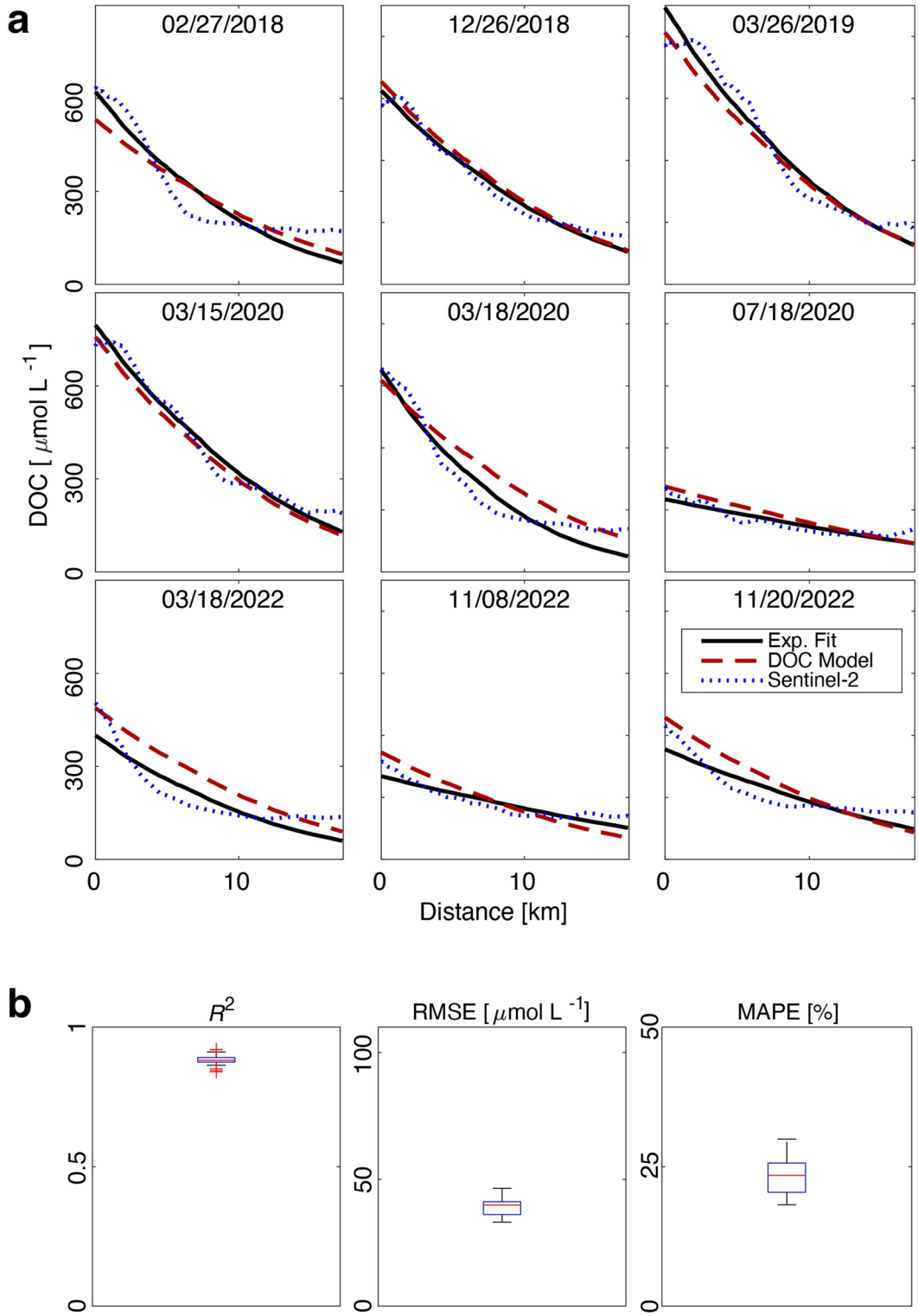

Figure 12. Performance assessment of the thalweg-DOC model using the Sentinel-2 scenes selected for model validation. (a) Comparison of dissolved organic carbon (DOC) concentrations derived from the thalweg-DOC model (dashed red line), the corresponding exponential fitted curve (black line), and Sentinel-2 (dashed blue line) along the Plum Island Estuary thalweg transect for an example set of nine independent Sentinel-2 scenes selected for model validation. In this case, the nine independent scenes are the ones presented in Figures 8 and 9. (b) Boxplots of accuracy assessment metrics—R^2, RMSE, MAPE–derived from the comparison of modeled and Sentinel-2 derived DOC transects. The metrics shown here are summaries of the 31 cross-validations.

Most importantly, the final *thalweg-DOC model* was able to reproduce the measured in situ DOC concentrations along the thalweg within ±16% (Figure 13). A set of 75 *in situ* DOC measurements (unused in the algorithm and model development) collected along the entire thalweg between 2017 and 2023 provided a valuable independent data set to conduct an end-to-end validation of the model's performance. The sample locations were homogeneously distributed across the estuary (Figure 13a), and this validation data set covered a measured DOC concentration range of about 100–600 μmol L^{-1}, which was representative for this system. It also encompassed data from different years and seasons although it was heavily represented by 2018 and 2022. The model was able to reproduce about 80% (R^2 = 0.79) of the variability in the in situ DOC, and estimates were on average within ±47 μmol L^{-1} or ±15.9% of the measured values, as indicated by the RMSE and MAPE (Figure 13b). The estimates were also uniformly distributed around the 1-to-1 line, indicating no major bias in the estimates. Although further assessment is needed to test the performance of the model during episodic or extreme events, this end-to-end validation provided great confidence in the reliability of *thalweg-DOC model* made for predicting point DOC concentration under most environmental conditions.

Implementation of the *thalweg-DOC model* for a continuous period of three years (1 January 2020–31 December 2022; 15-min time step) provided a realistic representation of DOC dynamics in this tidal estuary (Figure 14). Implementing the model over multiple years demonstrated the effects of the tidal, seasonal, and interannual variability in the drivers on the DOC concentrations (Figure 14a). For instance, the Parker River hydrograph showed considerable interannual variability across these 3 years. The variability in modeled DOC concentrations was investigated for three stations distributed along the thalweg: Upstream (Stn1), Middle of estuary (Stn2), and Near mouth (Stn3). As expected, the average and range of modeled DOC were greatest at Stn1 (223–762 μmol L^{-1}), which was directly influenced by the Parker River, and decreased progressively toward Stn2 (151–448 μmol L^{-1}) and Stn3 (89–220 μmol L^{-1}). At each station, the model adequately reproduced the diurnal oscillations in DOC concentration resulting from tidal forcing, as well as the enhanced range of variability typically associated with spring tides (Menendez et al., 2022; Nascimento et al., 2021). The modeled DOC concentration also clearly increased during periods of enhanced discharge, again following expectations (Zarnetske et al., 2018). Finally, the effects of the EVI2 seasonality were most evident in the fall, when DOC concentrations rose steadily as the EVI2 decreases.

5. Concluding Remarks

This study demonstrated that HSRRS can facilitate the accurate monitoring of DOC concentrations in tidal marsh-influenced estuaries, and provide critical data to inform and validate simple models of DOC dynamics in these hydrodynamically and biogeochemically complex systems. The Sentinel-2A/B tandem and its 5-day revisit time supplied a high-quality, clear-sky snapshot of DOC concentrations in the PIE every 16 days on average. Over a period of 6 years (2017–2023) this acquisition frequency was sufficient to capture a set of DOC spatial distributions representative of most environmental conditions encountered in this system (e.g., tidal stage, river discharge, marsh biomass). This collection helped identify the primary drivers of DOC variability and facilitated the training of a simple statistical model capable of predicting accurate DOC distributions along the estuary from three environmental variables. Although the proposed model is expected to provide reasonable DOC estimates during conditions beyond those used to train the model, the actual model's performance during extreme events such as large storms (e.g., Nor'easters, Hurricanes) remains unknown, and requires further assessments using field measurements. The general approach presented here can be applied to other tidal marsh-influenced estuaries, although algorithms and model parameters would probably need to be tuned and validated for specific systems or regions. Other environmental variables such as soil type and organic carbon content, terrain steepness, saltmarsh type and surface area, and climate are all factors that could potentially influence DOC concentrations across different marsh-influenced estuaries. Expanding this study to other estuarine systems across a latitudinal gradient would help assess the predictive capabilities of these other environmental variables and potentially help develop more broadly applicable models. This kind of simple DOC models can be coupled with the outputs of hydrodynamic models and facilitate the calculation of realistic DOC fluxes in these dynamic systems, and their implementation on large scales could help fill an important gap in regional and global carbon cycle models.

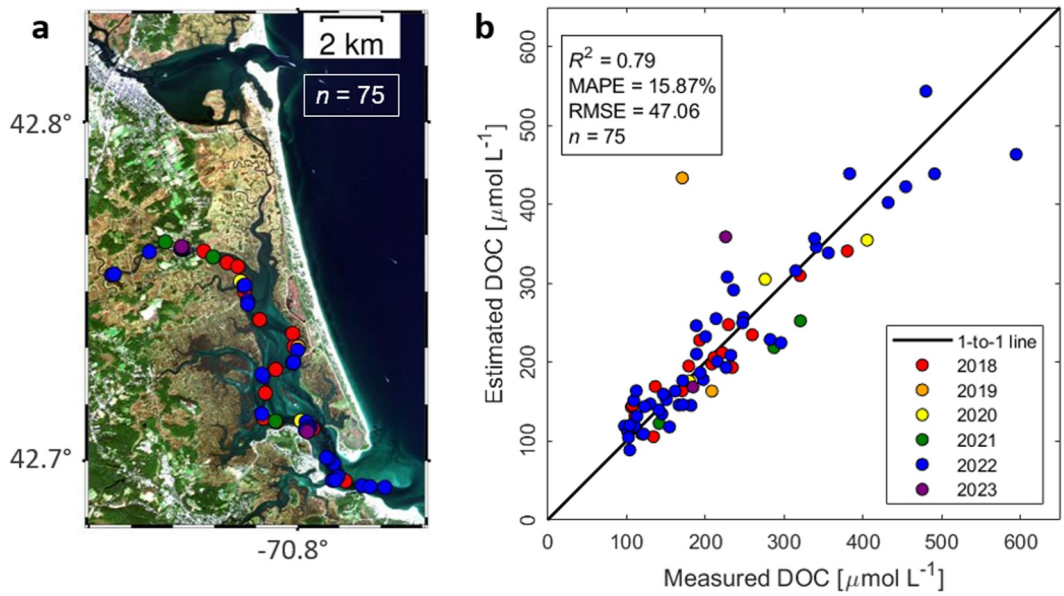

Figure 13. Validation of the *thalweg-DOC model* using in situ measurements of dissolved organic carbon (DOC) concentration collected within 200 m of the thalweg during the 2017–2023 time period. (a) Map showing the exact geographic locations of the samples used in this thalweg-DOC model validation, along the thalweg. (b) DOC concentrations estimated (*Estimated DOC*) using the *thalweg-DOC model* (Parker River Discharge, Marsh enhanced vegetation index 2, Water Level as predictors), versus DOC concentration measured in the laboratory (*Measured DOC*) on samples collected within 200 m of the thalweg.

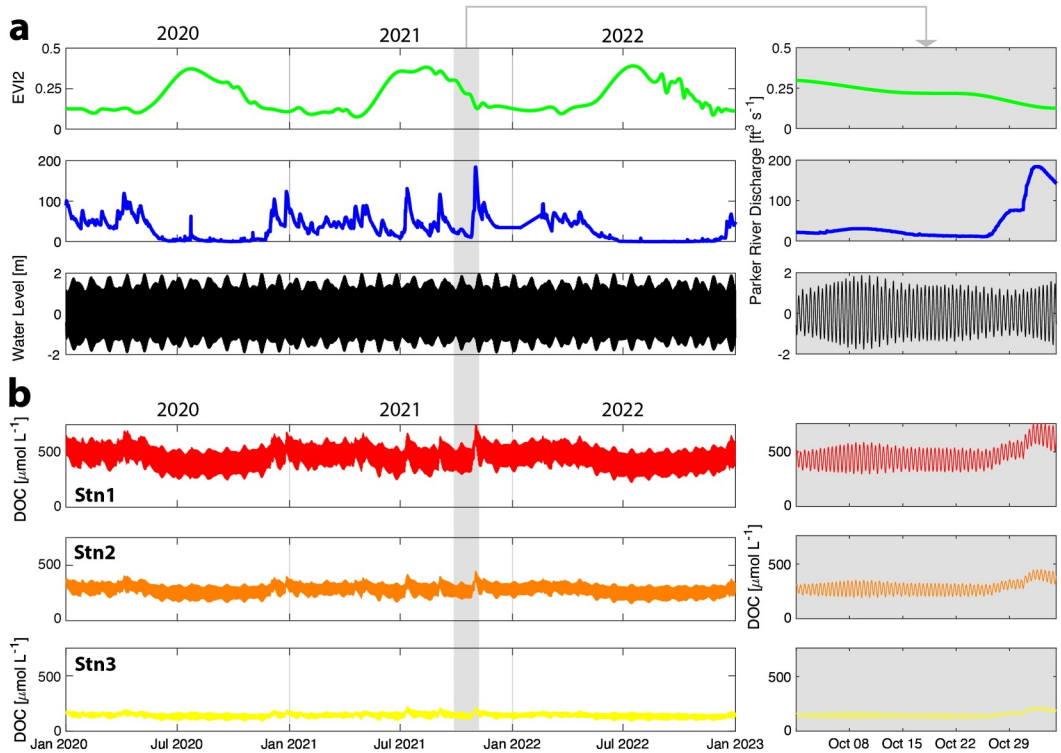

Figure 14. Implementation of the thalweg-DOC model for 2020–2022 at three locations along the thalweg transect. (a) Time series (15-min time step) of the three predictors used to model dissolved organic carbon (DOC) concentrations along the Plum Island Estuary (PIE) thalweg: Saltmarsh enhanced vegetation index 2 (EVI2) (green line), Parker River discharge (blue line), and water level (WL) (black line). Close-up views of the time series during October 2021 (gray shaded area) are shown on the right. (b) Time series (15-min time step) of the DOC concentration predicted from the Saltmarsh EVI2, Parker River discharge, and WL (multiple linear regression model) at three different locations along the thalweg: Stn1 located upstream and at the mouth of the Parker River (red line), at approximately 2.4 km from the beginning of the thalweg. Stn2 located in the middle of the Plum Island Sound (orange line), at approximately 7 km. Stn3 located near the mouth of the PIE (yellow line), at approximately 13 km.

Data Availability Statement

The Sentinel-2 images are available at the CNES PEPS website (https://peps.cnes.fr) (CNES, n.d.) (Dataset). The relative spectral responses of the Sentinel-2 MSI are available from the Copernicus website (https://sentinels.copernicus.eu/web/sentinel/user-guides/sentinel-2-msi/document-library/-/asset_publisher/Wk0TKajiISaR/content/sentinel-2a-spectral-response) (ESA, 2023) (Dataset). The Parker River discharge data is available at USGS website (https://waterdata.usgs.gov/nwis/uv?site_no=01101000) (USGS, n.d.) (Dataset). Water level data is available at NOAA website (https://tidesandcurrents.noaa.gov/stationhome.html?id=8441241) NOAA. (n.d.) (Dataset). The extent of the PIE marsh area is available at the National Wetland Inventory (USGS, 2023) (Dataset). The version 20221114.0 of the ACOLITE available at Institute of Natural Sciences website (https://odnature.naturalsciences.be/remsem/software-and-data/acolite) (Vanhellemont, 2019; OD Nature, n.d.) (Software). Maps were created using ArcGIS® PRO (commercial) (Esri, n.d.) (Software) and the Generic Mapping Tools available at(https://www.generic-mapping-tools.org) (Wessel et al., 2019; GMT, n.d.) (Software). MatLAB® (MathWorks, 2021) and ArcGIS® PRO (Esri, n.d.) softwares were used under licenses obtained by Boston University and Istanbul Technical University (Software). Field measurements of DOC concentration, CDOM absorption coefficient, and spectral remote-sensing reflectance along with the corresponding coordinates, dates and times of collection are available in an excel spreadsheet available at the following Zenodo repository (https://doi.org/10.5281/zenodo.13769438) (Dataset).

Acknowledgments
The authors declare no competing financial interest. Financial support for this work was directly provided by the National Science Foundation Plum Island Ecosystems Long-Term Ecological Research Program (OCE-2224608), and was partially supported by a NASA Remote Sensing of Water Quality Grant (80NSSC18K0344) to CGF and a Future Investigators in NASA Earth and Space Science and Technology Grant (80NSSC20K1648) to JPH (FI) and CGF (PI). The authors also acknowledge the Boston University Undergraduate Research Opportunities Program for its support of OCG and JS during the summers of 2019 and 2022, and the Boston University Warren McLeod Fund for supporting MWW during the summer 2022. Finally, the authors acknowledge the financial support of the Scientific and Technological Research Council of Türkiye under project number 1059B142200399 (TUBITAK-2214/A Grant Program). We would like to thank Lucas Florsheim, Carly Baracco, and Huan Mi for assistance with some sample and data collection. We also thank the Boston University Marine Program and the marine semester students enrolled in the 2017, 2019, and 2021 Bio-Optical Oceanography class, and the crews of the NOAA R/V Auk and UNH R/V Gulf Challenger for their support with logistics and sample collection. Finally, we thank the European Space Agency for providing free access to the Sentinel-2 imagery.

References

Antoine, D., Hooker, S. B., Bélanger, S., Matsuoka, A., & Babin, M. (2013). Apparent optical properties of the Canadian Beaufort Sea - Part 1: Observational overview and water column relationships. *Biogeosciences*, *10*(7), 4493–4509. https://doi.org/10.5194/bg-10-4493-2013

Araújo, C. A. S., & Bélanger, S. (2022). Variability of bio-optical properties in nearshore waters of the estuary and Gulf of St. Lawrence: Absorption and backscattering coefficients. *Estuarine, Coastal and Shelf Science*, *264*, 107688. https://doi.org/10.1016/J.ECSS.2021.107688

Avery, G. B., Kieber, R. J., Willey, J. D., Shank, G. C., & Whitehead, R. F. (2004). Impact of hurricanes on the flux of rainwater and Cape Fear River water dissolved organic carbon to Long Bay, southeastern United States. *Global Biogeochemical Cycles*, *18*(3). https://doi.org/10.1029/2004GB002229

Bauer, J. E., Cai, W. J., Raymond, P. A., Bianchi, T. S., Hopkinson, C. S., & Regnier, P. A. G. (2013). The changing carbon cycle of the coastal ocean. *Nature*, *504*(7478), 61–70. https://doi.org/10.1038/NATURE12857

Benway, H. M., Alin, S. R., Boyer, E., Cai, W.-J., Coble, P. G., Cross, J. N., et al. (2016). A science plan for carbon cycle research in North American coastal waters. *Report of the Coastal CARbon Synthesis (CCARS) community workshop*, (pp. 19–21). https://doi.org/10.1575/1912/7777

Bianchi, T. S. (2011). The role of terrestrially derived organic carbon in the coastal ocean: A changing paradigm and the priming effect. *Proceedings of the National Academy of Sciences of the United States of America*, *108*(49), 19473–19481. https://doi.org/10.1073/pnas.1017982108

Bianchi, T. S., Filley, T., Dria, K., & Hatcher, P. G. (2004). Temporal variability in sources of dissolved organic carbon in the lower Mississippi river. *Geochimica et Cosmochimica Acta*, *68*(5), 959–967. https://doi.org/10.1016/J.GCA.2003.07.011

Bianchi, T. S., Garcia-Tigreros, F., Yvon-Lewis, S. A., Shields, M., Mills, H. J., Butman, D., et al. (2013). Enhanced transfer of terrestrially derived carbon to the atmosphere in a flooding event. *Geophysical Research Letters*, *40*(1), 116–122. https://doi.org/10.1029/2012GL054145

Bolton, D. K., Gray, J. M., Melaas, E. K., Moon, M., Eklundh, L., & Friedl, M. A. (2020). Continental-scale land surface phenology from harmonized Landsat 8 and Sentinel-2 imagery. *Remote Sensing of Environment*, *240*, 111685. https://doi.org/10.1016/j.rse.2020.111685

Brewin, R. J. W., Sathyendranath, S., Kulk, G., Rio, M. H., Concha, J. A., Bell, T. G., et al. (2023). Ocean carbon from space: Current status and priorities for the next decade. *Earth-Science Reviews*, *240*, 104386. https://doi.org/10.1016/j.earscirev.2023.104386

Cai, Y., Guo, L., Wang, X., & Aiken, G. (2015). Abundance, stable isotopic composition, and export fluxes of DOC, POC, and DIC from the Lower Mississippi River during 2006–2008. *Journal of Geophysical Research: Biogeosciences*, *120*(11), 2273–2288. https://doi.org/10.1002/2015jg003139

Cao, F., & Tzortziou, M. (2021). Capturing dissolved organic carbon dynamics with Landsat-8 and Sentinel-2 in tidally influenced wetland–estuarine systems. *Science of the Total Environment*, *777*, 145910. https://doi.org/10.1016/J.SCITOTENV.2021.145910

Cao, F., Tzortziou, M., Hu, C., Mannino, A., Fichot, C. G., Del Vecchio, R., et al. (2018). Remote sensing retrievals of colored dissolved organic matter and dissolved organic carbon dynamics in North American estuaries and their margins. *Remote Sensing of Environment*, *205*, 151–165. https://doi.org/10.1016/j.rse.2017.11.014

CEC. (2016). North America's blue carbon: Assessing seagrass, salt marsh and mangrove distribution and carbon sinks project report commission for environmental cooperation.

Chalmers, A. G., Wiegert, R. G., & Wolf, P. L. (1985). Carbon balance in a salt marsh: Interactions of diffusive export, tidal deposition and rainfall-caused erosion. *Estuarine, Coastal and Shelf Science*, *21*(6), 757–771. https://doi.org/10.1016/0272-7714(85)90071-X

ChunHock, S., Cherukuru, N., Mujahid, A., Martin, P., Sanwlani, N., Warneke, T., et al. (2020). A new remote sensing method to estimate river to ocean DOC flux in peatland dominated Sarawak coastal regions, Borneo. *Remote Sensing*, *12*(20), 3380. https://doi.org/10.3390/RS12203380

Clark, J. B., Long, W., Tzortziou, M., Neale, P. J., & Hood, R. R. (2018). Wind-driven dissolved organic matter dynamics in a Chesapeake bay tidal marsh-estuary system. *Estuaries and Coasts*, *41*(3), 708–723. https://doi.org/10.1007/S12237-017-0295-1/FIGURES/9

CNES. (n.d.). Peps [Dataset]. https://peps.cnes.fr/

Cronin-Golomb, O., Harringmeyer, J. P., Weiser, M. W., Zhu, X., Ghosh, N., Novak, A. B., et al. (2022). Modeling benthic solar exposure (UV and visible) in dynamic coastal systems to better inform seagrass habitat suitability. *Science of the Total Environment*, *812*, 151481. https://doi.org/10.1016/J.SCITOTENV.2021.151481

Del Vecchio, R., & Blough, N. V. (2004). Spatial and seasonal distribution of chromophoric dissolved organic matter and dissolved organic carbon in the Middle Atlantic Bight. *Marine Chemistry*, *89*(1–4), 169–187. https://doi.org/10.1016/J.MARCHEM.2004.02.027

Duarte, C. M., Middelburg, J. J., & Caraco, N. (2005). Major role of marine vegetation on the ocean carbon cycle. *Biogeosciences*, *1*, 1–8. https://doi.org/10.5194/bg-2-1-2005

ESA. (2015). Sentinel-2 user handbook. In *Sentinel user handbook and exploitation Tools (issue 1)*. https://doi.org/10.1021/ie51400a018

ESA. (2023). Sentinel-2 spectral response functions (S2-SRF) - Sentinel online [Dataset]. *COPE-GSEG-EOPG-TN-15-0007*. Retrieved from https://sentinels.copernicus.eu/web/sentinel/user-guides/sentinel-2-msi/document-library/-/asset_publisher/Wk0TKajiISaR/content/sentinel-2a-spectral-responses

Esri. (n.d.). [Software]. *ArcGIS Pro*. Retrieved from https://www.esri.com/en-us/arcgis/products/arcgis-pro/overview

Fagherazzi, S., Mariotti, G., Banks, A. T., Morgan, E. J., & Fulweiler, R. W. (2014). The relationships among hydrodynamics, sediment distribution, and chlorophyll in a mesotidal estuary. *Estuarine, Coastal and Shelf Science*, *144*, 54–64. https://doi.org/10.1016/j.ecss.2014.04.003

Fell, F. (2022). A contrast minimization approach to remove sun glint in landsat 8 imagery. *Remote Sensing*, *14*(18), 4643. https://doi.org/10.3390/RS14184643

Fichot, C. G., & Benner, R. (2011). A novel method to estimate DOC concentrations from CDOM absorption coefficients in coastal waters. *Geophysical Research Letters*, *38*(3). https://doi.org/10.1029/2010GL046152

Fichot, C. G., & Benner, R. (2012). The spectral slope coefficient of chromophoric dissolved organic matter (S 275-295) as a tracer of terrigenous dissolved organic carbon in river-influenced ocean margins. *Limnology & Oceanography*, *57*(5), 1453–1466. https://doi.org/10.4319/LO.2012.57.5.1453

Fichot, C. G., & Benner, R. (2014). The fate of terrigenous dissolved organic carbon in a river-influenced ocean margin. *Global Biogeochemical Cycles*, *28*(3), 300–318. https://doi.org/10.1002/2013GB004670

Fichot, C. G., Harringmeyer, J., & Weiser, M. (2022). *Delta-X: In situ water quality indicators across MRD, LA, USA, 2021, version 2*. ORNL Distributed Active Archive Center. https://doi.org/10.3334/ORNLDAAC/2080

Fichot, C. G., Lohrenz, S. E., & Benner, R. (2014). Pulsed, cross-shelf export of terrigenous dissolved organic carbon to the Gulf of Mexico. *Journal of Geophysical Research: Oceans*, *119*(2), 1176–1194. https://doi.org/10.1002/2013JC009424

Fichot, C. G., Tzortziou, M., & Mannino, A. (2023). Remote sensing of dissolved organic carbon (DOC) stocks, fluxes and transformations along the land-ocean aquatic continuum: Advances, challenges, and opportunities. *Earth-Science Reviews*, *242*, 104446. https://doi.org/10.1016/j.earscirev.2023.104446

Forbrich, I., Giblin, A. E., & Hopkinson, C. S. (2018). Constraining marsh carbon budgets using long-term C burial and contemporary atmospheric CO2 fluxes. *Journal of Geophysical Research: Biogeosciences*, *123*(3), 867–878. https://doi.org/10.1002/2017JG004336

Gattuso, J. P., Frankignoulle, M., & Wollast, R. (1998). Carbon and carbonate metabolism in coastal aquatic ecosystems. *Annual Review of Ecology and Systematics*, *29*(1), 405–434. https://doi.org/10.1146/annurev.ecolsys.29.1.405

GMT. (n.d.). The generic mapping tools [Software]. https://www.generic-mapping-tools.org

Gordon, H. R., & Ding, K. (1992). Self-shading of in-water optical instruments. *Limnology & Oceanography*, *37*(3), 491–500. https://doi.org/10.4319/LO.1992.37.3.0491

Harmel, T., Chami, M., Tormos, T., Reynaud, N., & Danis, P. A. (2018). Sunglint correction of the Multi-Spectral Instrument (MSI)-SENTINEL-2 imagery over inland and sea waters from SWIR bands. *Remote Sensing of Environment*, *204*, 308–321. https://doi.org/10.1016/J.RSE.2017.10.022

Harringmeyer, J. P., Ghosh, N., Weiser, M. W., Thompson, D. R., Simard, M., Lohrenz, S. E., & Fichot, C. G. (2024). A hyperspectral view of the nearshore Mississippi River Delta: Characterizing suspended particles in coastal wetlands using imaging spectroscopy. *Remote Sensing of Environment*, *301*, 113943. https://doi.org/10.1016/J.RSE.2023.113943

Hedges, J. I., Keil, R. G., & Benner, R. (1997). What happens to terrestrial organic matter in the ocean? *Organic Geochemistry*, *27*(5–6), 195–212. https://doi.org/10.1016/S0146-6380(97)00066-1

Herrmann, M., Najjar, R. G., Kemp, W. M., Alexander, R. B., Boyer, E. W., Cai, W. J., et al. (2015). Net ecosystem production and organic carbon balance of U.S. East coast estuaries: A synthesis approach. *Global Biogeochemical Cycles*, *29*(1), 96–111. https://doi.org/10.1002/2013GB004736

Hooker, S. B., Morrow, J. H., & Matsuoka, A. (2013). Apparent optical properties of the Canadian Beaufort Sea - Part 2: The 1% and 1 cm perspective in deriving and validating AOP data products. *Biogeosciences*, *10*(7), 4511–4527. https://doi.org/10.5194/bg-10-4511-2013

Hopkinson, C. S., Morris, J. T., Fagherazzi, S., Wollheim, W. M., & Raymond, P. A. (2018). Lateral marsh edge erosion as a source of sediments for vertical marsh accretion. *Journal of Geophysical Research: Biogeosciences*, *123*(8), 2444–2465. https://doi.org/10.1029/2017JG004358

Hounshell, A. G., Rudolph, J. C., Van Dam, B. R., Hall, N. S., Osburn, C. L., & Paerl, H. W. (2019). Extreme weather events modulate processing and export of dissolved organic carbon in the Neuse River Estuary, NC. *Estuarine, Coastal and Shelf Science*, *219*, 189–200. https://doi.org/10.1016/J.ECSS.2019.01.020

Jiang, Z., Huete, A. R., Didan, K., & Miura, T. (2008). Development of a two-band enhanced vegetation index without a blue band. *Remote Sensing of Environment*, *112*(10), 3833–3845. https://doi.org/10.1016/j.rse.2008.06.006

Joshi, I. D., D'Sa, E. J., Osburn, C. L., Bianchi, T. S., Ko, D. S., Oviedo-Vargas, D., et al. (2017). Assessing chromophoric dissolved organic matter (CDOM) distribution, stocks, and fluxes in Apalachicola Bay using combined field, VIIRS ocean color, and model observations. *Remote Sensing of Environment*, *191*, 359–372. https://doi.org/10.1016/J.RSE.2017.01.039

Juhls, B., Paul Overduin, P., Hölemann, J., Hieronymi, M., Matsuoka, A., Heim, B., & Fischer, J. (2019). Dissolved organic matter at the fluvial-marine transition in the Laptev Sea using in situ data and ocean colour remote sensing. *Biogeosciences*, *16*(13), 2693–2713. https://doi.org/10.5194/BG-16-2693-2019

Keith, D. J., Lunetta, R. S., & Schaeffer, B. A. (2016). Optical models for remote sensing of colored dissolved organic matter absorption and salinity in new England, middle Atlantic and Gulf coast estuaries USA. *Remote Sensing*, *8*(4), 283. https://doi.org/10.3390/rs8040283

Logozzo, L., Tzortziou, M., Neale, P., & Clark, J. B. (2021). Photochemical and microbial degradation of chromophoric dissolved organic matter exported from tidal marshes. *Journal of Geophysical Research: Biogeosciences*, *126*(4). https://doi.org/10.1029/2020JG005744

Mabit, R., Araújo, C. A. S., Singh, R. K., & Bélanger, S. (2022). Empirical remote sensing algorithms to retrieve SPM and CDOM in québec coastal waters. *Frontiers in Remote Sensing*, *3*, 834908. https://doi.org/10.3389/FRSEN.2022.834908

Macreadie, P. I., Hughes, A. R., & Kimbro, D. L. (2013). Loss of "blue carbon" from coastal salt marshes following habitat disturbance. *PLoS One*, *8*(7), 1–8. https://doi.org/10.1371/journal.pone.0069244

Mannino, A., Russ, M. E., & Hooker, S. B. (2008). Algorithm development and validation for satellite-derived distributions of DOC and CDOM in the U.S. Middle Atlantic Bight. *Journal of Geophysical Research*, *113*(7). https://doi.org/10.1029/2007JC004493

Mannino, A., Signorini, S. R., Novak, M. G., Wilkin, J., Friedrichs, M. A. M., & Najjar, R. G. (2016). Dissolved organic carbon fluxes in the Middle Atlantic Bight: An integrated approach based on satellite data and ocean model products. *Journal of Geophysical Research: Biogeosciences*, *121*(2), 312–336. https://doi.org/10.1002/2015JG003031

MathWorks. (2021). MATLAB (version R2021b) [Software]. https://www.mathworks.com/products/matlab.html

Matsuoka, A., Boss, E., Babin, M., Karp-Boss, L., Hafez, M., Chekalyuk, A., et al. (2017). Pan-Arctic optical characteristics of colored dissolved organic matter: Tracing dissolved organic carbon in changing Arctic waters using satellite ocean color data. *Remote Sensing of Environment*, *200*, 89–101. https://doi.org/10.1016/J.RSE.2017.08.009

McLeod, E., Chmura, G. L., Bouillon, S., Salm, R., Björk, M., Duarte, C. M., et al. (2011). A blueprint for blue carbon: Toward an improved understanding of the role of vegetated coastal habitats in sequestering CO2. *Frontiers in Ecology and the Environment*, *9*(10), 552–560. https://doi.org/10.1890/110004

Medeiros, P. M. (2022). The effects of hurricanes and storms on the composition of dissolved organic matter in a southeastern U.S. Estuary. *Frontiers in Marine Science*, *9*, 855720. https://doi.org/10.3389/FMARS.2022.855720/BIBTEX

Menendez, A., Tzortziou, M., Neale, P., Megonigal, P., Powers, L., Schmitt-Kopplin, P., & Gonsior, M. (2022). Strong dynamics in tidal marsh DOC export in response to natural cycles and episodic events from continuous monitoring. *Journal of Geophysical Research: Biogeosciences*, *127*(7), e2022JG006863. https://doi.org/10.1029/2022JG006863

Moran, M. A., Sheldon, W. M., & Sheldon, J. E. (1999). Biodegradation of riverine dissolved organic carbon in five estuaries of the southeastern United States. *Estuaries*, *22*(1), 55–64. https://doi.org/10.2307/1352927/METRICS

Morris, J. T., Sundberg, K., & Hopkinson, C. S. (2013). Salt marsh primary production and its responses to relative sea level and nutrientsin estuaries at plum island, Massachusetts, and North Inlet, South Carolina, USA. *Oceanography*, *26*(3), 78–84. https://doi.org/10.5670/oceanog.2013.48

Nahlik, A. M., & Fennessy, M. S. (2016). Carbon storage in US wetlands. *Nature Communications*, *7*, 1–9. https://doi.org/10.1038/ncomms13835

Najjar, R. G., Herrmann, M., Alexander, R., Boyer, E. W., Burdige, D. J., Butman, D., et al. (2018). Carbon budget of tidal wetlands, estuaries, and shelf waters of eastern North America. *Global Biogeochemical Cycles*, *32*(3), 389–416. https://doi.org/10.1002/2017GB005790

Nascimento, Â., Biguino, B., Borges, C., Cereja, R., Cruz, J. P. C., Sousa, F., et al. (2021). Tidal variability of water quality parameters in a mesotidal estuary (Sado Estuary, Portugal). *Scientific Reports*, *11*(1), 23112. https://doi.org/10.1038/s41598-021-02603-6

Neeley, A. R., & Mannino, A. (2018). IOCCG protocol series (2018). Inherent optical property measurements and protocols: Absorption coefficient. In *IOCCG ocean optics and biogeochemistry protocols for satellite ocean colour sensor validation* (Vol. 1). https://doi.org/10.25607/OBP-119

NOAA. (n.d.). Tides and currents [Dataset]. https://tidesandcurrents.noaa.gov/stationhome.html?id=8441241

OD Nature. (n.d.). Acolite [Software]. https://odnature.naturalsciences.be/remsem/software-and-data/acolite

Osburn, C. L., Rudolph, J. C., Paerl, H. W., Hounshell, A. G., & Van Dam, B. R. (2019). Lingering carbon cycle effects of hurricane Matthew in North Carolina's coastal waters. *Geophysical Research Letters*, *46*(5), 2654–2661. https://doi.org/10.1029/2019GL082014

Pérez-Rodríguez, M., & Biester, H. (2022). Sensitivity of river catchments to discharge-controlled dissolved carbon export: A study of eight catchments in southern patagonia. *Biogeochemistry*, *160*(2), 177–197. https://doi.org/10.1007/S10533-022-00947-3/FIGURES/9

Qi, Y., Xue, Y., & Wang, X. (2017). Release and microbial degradation of dissolved organic carbon and nitrogen from Phragmites australis and Suaeda salsa in the wetland of the Yellow River Estuary. *Journal of Oceanography and Marine Research*, *5*(02), 2. https://doi.org/10.4172/2572-3103.1000160

Raymond, P. A., & Hopkinson, C. S. (2003). Ecosystem modulation of dissolved carbon age in a temperate marsh-dominated estuary. *Ecosystems*, *6*(7), 694–705. https://doi.org/10.1007/S10021-002-0213-6/TABLES/3

Raymond, P. A., & Saiers, J. E. (2010). Event controlled DOC export from forested watersheds. *Biogeochemistry*, *100*(1), 197–209. https://doi.org/10.1007/s10533-010-9416-7

Schiebel, H. N., Gardner, G. B., Wang, X., Peri, F., & Chen, R. F. (2018). Seasonal export of dissolved organic matter from a new England salt marsh. *Journal of Coastal Research*, *34*(4), 939–954. https://doi.org/10.2112/JCOASTRES-D-16-00196.1

Shelton, S., Neale, P., Pinsonneault, A., & Tzortziou, M. (2022). Biodegradation and photodegradation of vegetation-derived dissolved organic matter in tidal marsh ecosystems. *Estuaries and Coasts*, *45*(5), 1324–1342. https://doi.org/10.1007/S12237-021-00982-7/FIGURES/10

Signorini, S. R., Mannino, A., Friedrichs, M. A. M., St-Laurent, P., Wilkin, J., Tabatabai, A., et al. (2019). Estuarine dissolved organic carbon flux from space: With application to Chesapeake and Delaware bays. *Journal of Geophysical Research: Oceans*, *124*(6), 3755–3778. https://doi.org/10.1029/2018JC014646

Smith, S. V., & Hollibaugh, J. T. (1993). Coastal metabolism and the oceanic organic carbon balance. *Reviews of Geophysics*, *31*(1), 75–89. https://doi.org/10.1029/92rg02584

Stramski, D., Reynolds, R. A., Kaczmarek, S., Uitz, J., & Zheng, G. (2015). Correction of pathlength amplification in the filter-pad technique for measurements of particulate absorption coefficient in the visible spectral region. *Applied Optics*, *54*(22), 6763. https://doi.org/10.1364/ao.54.006763

Tzortziou, M., Neale, P. J., Osburn, C. L., Megonigal, J. P., Maie, N., & Jaffé, R. (2008). Tidal marshes as a source of optically and chemically distinctive colored dissolved organic matter in the Chesapeake Bay. *Limnology & Oceanography*, *53*(1), 148–159. https://doi.org/10.4319/LO.2008.53.1.0148

Uhlenhopp, A. G., Hobbie, J. E., & Vallino, J. J. (1995). Effects of land use on the degradability of dissolved organic matter in three watersheds of the Plum Island Sound estuary. *The Biological Bulletin*, *189*(2), 256–257. https://doi.org/10.1086/BBLV189N2P256

USGS. (n.d.). Parker River at Byfield, MA – 01101000 [Dataset]. https://waterdata.usgs.gov/monitoring-location/01101000/#parameterCode=00065&period=P7D&showMedian=false

USGS. (2023). National wetlands inventory – Wetlands mapper [Dataset]. *National Wetlands Inventory*. Retrieved from https://fwsprimary.wim.usgs.gov/wetlands/apps/wetlands-mapper/

Vallino, J. J., & Hopkinson, C. S. (1998). Estimation of dispersion and characteristic mixing times in plum island Sound estuary. *Estuarine, Coastal and Shelf Science*, *46*(3), 333–350. https://doi.org/10.1006/ECSS.1997.0281

Vandermeulen, R. A., Mannino, A., Neeley, A., Werdell, J., & Arnone, R. (2017). Determining the optimal spectral sampling frequency and uncertainty thresholds for hyperspectral remote sensing of ocean color. *Optics Express*, *25*(16), A785. https://doi.org/10.1364/oe.25.00a785

Vanhellemont, Q. (2019). Adaptation of the dark spectrum fitting atmospheric correction for aquatic applications of the Landsat and Sentinel-2 archives. *Remote Sensing of Environment*, *225*, 175–192. https://doi.org/10.1016/j.rse.2019.03.010

Weiser, M. W., Swanson, J., Ghosh, N., Hong, J., Harringmeyer, J. P., Kaiser, K., & Fichot, C. G. (2024). Improving estimates of dissolved organic carbon (DOC) concentration from in situ fluorescence measurements across estuaries and coastal wetlands. *Environmental Science and Technology*, *58*(21), 9213–9226. https://doi.org/10.1021/ACS.EST.3C10850/ASSET/IMAGES/LARGE/ES3C10850_0006.JPEG

Wessel, P., Luis, J. F., Uieda, L., Scharroo, R., Wobbe, F., Smith, W. H. F., & Tian, D. (2019). The generic mapping tools version 6. *Geochemistry, Geophysics, Geosystems*, *20*(11), 5556–5564. https://doi.org/10.1029/2019GC008515

Yan, G., Labonté, J. M., Quigg, A., & Kaiser, K. (2020). Hurricanes accelerate dissolved organic carbon cycling in coastal ecosystems. *Frontiers in Marine Science*, *7*, 489791. https://doi.org/10.3389/FMARS.2020.00248/BIBTEX

Zarnetske, J. P., Bouda, M., Abbott, B. W., Saiers, J., & Raymond, P. A. (2018). Generality of hydrologic transport limitation of watershed organic carbon flux across ecoregions of the United States. *Geophysical Research Letters*, *45*(21), 11–702. https://doi.org/10.1029/2018gl080005

Zhang, X., Fichot, C. G., Baracco, C., Guo, R., Neugebauer, S., Bengtsson, Z., et al. (2020). Determining the drivers of suspended sediment dynamics in tidal marsh-influenced estuaries using high-resolution ocean color remote sensing. *Remote Sensing of Environment*, *240*, 111682. https://doi.org/10.1016/J.RSE.2020.111682

Zhang, X., He, S., Shabani, A., Zhai, P.-W., & Du, K. (2017). Spectral sea surface reflectance of skylight. *Optics Express*, *25*(4), A1–A13. https://doi.org/10.1364/oe.25.0000a1

Zhang, X., Leonardi, N., Donatelli, C., & Fagherazzi, S. (2019). Fate of cohesive sediments in a marsh-dominated estuary. *Advances in Water Resources*, *125*, 32–40. https://doi.org/10.1016/J.ADVWATRES.2019.01.003

Zhao, L., Chen, C., Vallino, J., Hopkinson, C., Beardsley, R. C., Lin, H., et al. (2010). Wetland-estuarine-shelf interactions in the plum island Sound and Merrimack River in the Massachusetts coast. *Journal of Geophysical Research*, *115*(C10), 10039. https://doi.org/10.1029/2009JC006085

Zhu, X., Miller, W. L., & Fichot, C. G. (2020). Simple method to determine the apparent quantum yield matrix of CDOM photobleaching in natural waters. *Environmental Science and Technology*, *54*(21), 14096–14106. https://doi.org/10.1021/acs.est.0c03605

Zibordi, G., Mélin, F., Voss, K. J., Johnson, B. C., Franz, B. A., Kwiatkowska, E., et al. (2015). System vicarious calibration for ocean color climate change applications: Requirements for in situ data. *Remote Sensing of Environment*, *159*, 361–369. https://doi.org/10.1016/J.RSE.2014.12.015

Zibordi, G., Ruddick, K., Ansko, I., Moore, G., Kratzer, S., Icely, J., & Reinart, A. (2012). In situ determination of the remote sensing reflectance: An inter-comparison. *Ocean Science*, *8*(4), 567–586. https://doi.org/10.5194/OS-8-567-2012